The effect of variations in cooling rates on mineral compositions in mid-ocean ridge basalts

Journal Article

Author(s):
EIMF (Edinburgh Ion Microprobe Facility); McCarthy, Anders John (iD); Chelle-Michou, Cyril (iD); Blundy, Jonathan D.; Dorais, Michael J.; van der Zwan, Froukje M.; Peate, David W.
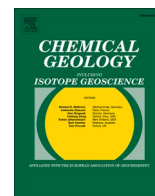
The effect of variations in cooling rates on mineral compositions in mid-ocean ridge basalts

Anders McCarthy [a,*], Cyril Chelle-Michou [a], Jonathan D. Blundy [b], Michael J. Dorais [c], Froukje M. van der Zwan [d,e], David W. Peate [f], EIMF (Edinburgh Ion Microprobe Facility)[g]

[a] Institute of Geochemistry and Petrology, Department of Earth Sciences, ETH Zürich, Clausiusstrasse 25, 8092 Zürich, Switzerland
[b] Department of Earth Sciences, University of Oxford, South Parks Road, Oxford OX1 3AN, UK
[c] Department of Geological Sciences, Brigham Young University, S-335 ESC, Provo, UT 84602, USA
[d] GEOMAR, Helmholtz Centre for Ocean Research, Kiel, Wischhofstraße 1-3, 24149 Kiel, Germany
[e] King Abdullah University of Science and Technology, Thuwal, Saudi Arabia
[f] Earth & Environmental Sciences, University of Iowa, 115 Trowbridge Hall, Iowa City, IA 52242, USA
[g] Grant Institute, University of Edinburgh, James Hutton Road, Kings Building, EH21 9FE, United Kingdom

ARTICLE INFO

ABSTRACT

We present textural and chemical analyses of minerals from a 150 m thick sequence of submarine mid-ocean ridge basalts from the South China Sea in order to showcase the effect of variations in magma cooling rates on mineral texture and mineral composition. Groundmass plagioclase and clinopyroxene show gradual changes in texture and composition as flows grade from slowly cooled, meter-thick massive flows to more rapidly cooled dm-thick pillow lobes with quenched glassy margins. The corresponding change in cooling-rate is estimated to vary from <1 to ≥ 100 °C/h. With increasing cooling rate, plagioclase forms elongated, sector-zoned swallow-tail crystals. Sector zoning is associated with increasing FeO (up to 1.5 wt%) and MgO (up to 0.6 wt%) abundances at near-constant anorthite (An), related to a two orders of magnitude increase in growth rate. Sr, Ba, Li and Ti abundances remain constant and appear unaffected by kinetic factors at such growth rates. With increasing cooling rate clinopyroxene becomes dendritic, and its composition is sensitive to changes in crystallization conditions. Increasing cooling rate (<1 to ≥ 100 °C/h) leads to increasing Al_2O_3 (average of 3.2 to 4.3 wt%), TiO_2 (1.3 to 2.8 wt%) and Na_2O (0.37 to 0.44 wt%) and a decrease in SiO_2 (50.1 to 46.4 wt%) and $Mg\#_{Fetot}$, i.e., molar $MgO/(MgO + FeO_{tot})$, from 71.3 to 53.1. Trace element abundances (Y, Zr, Ce, V, Sr) in clinopyroxene increase by up to an order of magnitude at cooling rates ≥ 100 °C/h and become more heterogeneous spatially. These results support experimental evidence that rapid crystal growth leads to significant departure of mineral compositions from equilibrium, in particular for clinopyroxene. Although plagioclase composition remains relatively insensitive to changes in growth conditions at the studied cooling rates, the sensitivity of clinopyroxene composition to growth rates imply that it should be used with caution as a tool to infer magmatic crystallization conditions.

1. Introduction

Constraining the parameters controlling growth, texture and composition of magmatic minerals is crucial in order to better constrain magmatic and volcanic processes, such as crystallization of magmatic bodies in the crust, changes in physico-chemical properties of magmas upon ascent and consequences for eruption dynamics (e.g. Blundy and Cashman, 2005; Di Genova et al., 2020; Arzilli et al., 2022).

The past decades have provided a wealth of information identifying

undercooling and crystallization kinetics as important factors controlling mineral textures and composition as a consequence of oversaturation induced by significant temperature-driven or degassing-induced undercooling (e.g. Hammer et al., 2010; Mollo and Hammer, 2017). This is particularly important in volcanic and subvolcanic systems, such as tephra, scoria, lava flows, lava tubes, as well as shallow dykes and sills, which are prone to disequilibrium growth conditions as a result of rapid cooling or volatile loss (e.g. Lesher et al., 1999; Blundy and Cashman, 2005; Shea and Hammer, 2013). Elevated undercooling

* Corresponding author.
E-mail address: anders.mccarthy@erdw.ethz.ch (A. McCarthy).

leading to changes in mineral composition and texture has been highlighted along dyke walls (Mollo et al., 2012), lava flows (Lesher et al., 1999; Zhou et al., 2000; Mollo et al., 2013a) and lava tubes (e.g. Lanzafame and Ferlito, 2014), as well as through experimental studies (e.g. Lofgren, 1974; Lofgren and Donaldson, 1975; Mollo et al., 2011a; Mollo et al., 2011b; Mollo et al., 2012; Shea and Hammer, 2013) and theoretical considerations (Albarede and Bottinga, 1972; Dowty, 1976a; Watson, 1996). Moreover, sector and dendritic zoning in magmatic olivine and clinopyroxene provide evidence of disequilibrium growth related to elevated growth rates in magmatic reservoirs (e.g. Dowty,

Fig. 1. a) Lithostratigraphy of basalts of IODP Exp. 367 Hole 1500B; b) High-resolution image of cored pillow lava with glassy, quenched margin; c) High-resolution image of cored hyaloclastites, showing mixed glassy basalt fragments mixed in with mudstone; figure modified from Larsen et al. (2018). For estimates of cooling rates, which will be used instead of slow, moderate, fast cooling for all following figures, see section 4.

1976b, Donaldson, 1977: Shimizu, 1990; O'Driscoll et al., 2007; Milman-Barris et al., 2008; Welsch et al., 2014; Arzilli et al., 2015; Hammer et al., 2016; McCarthy and Müntener, 2017; McCarthy et al., 2020). Indeed, shallow magmatic reservoirs, melt extraction zones, lava lakes, dykes and tephra are environments prone to disequilibrium, rapid crystal growth at rates that can be several orders of magnitude faster than for equilibrium crystallization (ca 10^6–10^7 cm/s versus 10^{10}–10^{11} cm/s respectively) (Cashman, 1993; Shea and Hammer, 2013) which strongly influence mineral compositions.

To provide further support for recent experimental work on the compositional evolution of minerals as a function of cooling rate (Mollo et al., 2010, Mollo et al., 2011a, Mollo et al., 2011a, Mollo et al., 2012, 2016, Pontesilli et al., 2019, Masotta et al., 2020) and on the effect of growth rates on the incorporation of trace elements in minerals (e.g. Mollo et al., 2013a, 2013b), we focus here on a series of basaltic lava flows emplaced at the ocean floor (mid-ocean ridge basalts, MORB) recovered during International Ocean Discovery Program (IODP) Expedition 367 (Larsen et al., 2018; Sun, Jian, Stock, Larsen, Klaus, and Alvarez Zarikian, 2018). We systematically target the internal and external segments of a series of thick lava flows and pillows and combine high-resolution mineral textures, microbeam chemical analysis of silicate phases and numerical modelling of cooling rates of lava flows upon emplacement as well as modelling of shifts in mineral composition (Mg in plagioclase) as a consequence of growth rates. We provide a large petrological and geochemical dataset that confirm how disequilibrium crystallization in response to high cooling rate has a significant impact on clinopyroxene and plagioclase texture, chemistry and zoning patterns, thereby highlighting the extent of compositional heterogeneity of silicate phases in volcanic products at the cm- to dm-scale.

2. Geological setting of site U1500B basalts

Thick aphyric to highly plagioclase phyric basaltic flows were recovered from IODP Exp. 367 (South China Sea) at Site U1500B (Stock et al., 2018; Sun, Jian, Stock, Larsen, Klaus, and Alvarez Zarikian, 2018) (Fig. 1). There are two distinct units with the upper ca. 27 m (*Unit 1a*) consisting of massive plagioclase ± olivine-phyric basalt lavas, and a lower unit (*Unit 1b*) consisting of ca. 123 m of alternating plagioclase-phyric pillow flows, thinner flows (lobate flows) and occasional thicker massive flows (Stock et al., 2018) (Fig. 1). *Unit 1a* is estimated to be formed of individual massive flows on the order of 7–8 m in thickness, whereas *Unit 1b* is dominated by 0.5–4.8 m thick lava flows *(supplementary appendix)* separated by similarly thick sequences of pillow basalts, with individual pillow lobes on about 0.5 m thick (Fig. 1b). Glassy margins of pillow lobes and hyaloclastites are locally well preserved, whereas glass within the groundmass is altered (Fig. 1b,c).

Mineralogy of the basalts is homogenous, with mm-sized plagioclase and olivine phenocrysts in a hypocrystalline groundmass of plagioclase, clinopyroxene, oxides and glass (Fig. 1, Fig. 2). Plagioclase can be subdivided into two distinct populations. The first consists of euhedral mm- to cm-size phenocrysts (0.1–2.5 cm in size, Stock et al., 2018) (Figs. 1b, 2b) found throughout the basalt flows. The second population, which makes up the groundmass as well as the rims of phenocrysts, shows either homogenous composition, normal core-rim zoning or sector zoning. Crystals in this population are characterized by a wide textural diversity, from blocky and euhedral in massive lava flows to acicular and swallow-tail habits with bow-fan and stellate arrangements in pillow basalts (Fig. 2c–e). Clinopyroxene (<0.5 mm) is found as a late-stage groundmass phase throughout the basalt flows except in the glassy, quenched margins of pillow lavas, where it is absent. Clinopyroxene is associated with elongated plagioclase, and forms either dendritic, skeletal grains in finer grained lava flows or blocky, subhedral grains in coarser grained flows leading to (sub)ophitic textures typical of massive lava flows and dolerites (Fig. 2c–e). Fresh olivine remains sparse in these lava flows, and is usually altered. When present, mm-size olivine phenocrysts are euhedral and chemically homogeneous.
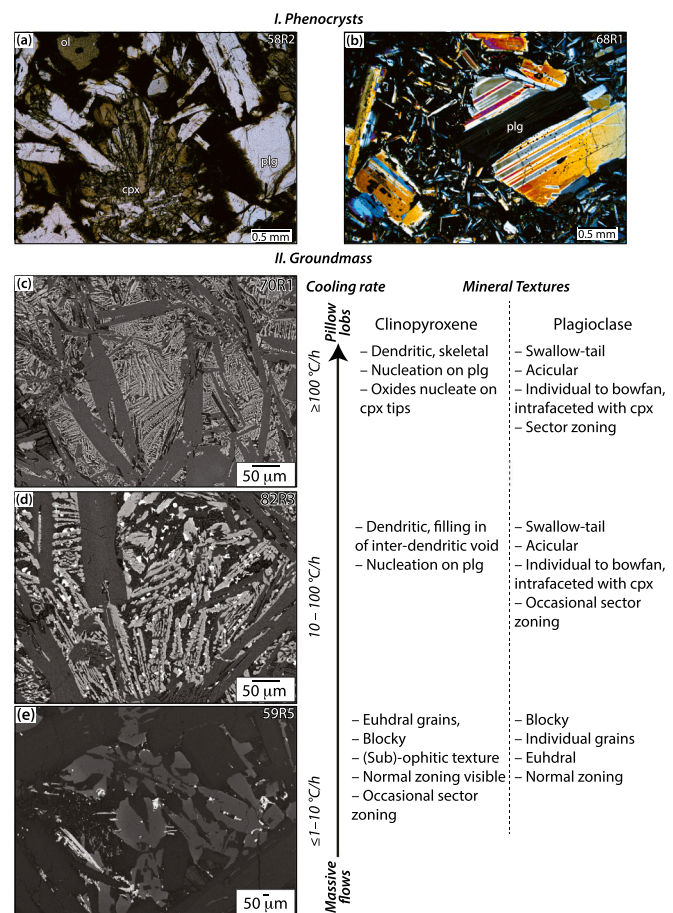

Fig. 2. Mineral textures of U1500 basalts: illustration of phenocrysts in thin sections (a) phenocrysts of plagioclase (plg) and olivine (ol) and a groundmass of clinopyroxene (cpx) and plagioclase (plain-polarized light) and (b) mm-large subhedral- to euhedral plagioclase (plg) phenocrysts within a groundmass of plagioclase and quenched glass (double-polarized light); zonations along the rims of plagioclase phenocrysts are visible. Groundmass texture of basalts are illustrated with SEM images and as a function of cooling rate (see discussion), ranging from pillow lobes (high cooling rate) to massive flows (low cooling rate): (c) Pillow lobe (rapidly cooled basalt) with a groundmass of dendritic- to swallow-tail plagioclase and dendritic clinopyroxene. Oxides are small (ca. 2 µm); (d) Moderately cooled basalt with a groundmass of coarser grained, elongated swallow-tail and acicular plagioclase and clinopyroxene and late-stage oxides; (f) Central section of a massive flow (slow cooled basalt), with a coarse-grained groundmass of euhedral plagioclase and interstitial clinopyroxene forming sub-ophitic textures. Oxides are generally anhedral to elongated and normal zoning is observed in both clinopyroxene and plagioclase. It is important to stress that these estimated cooling rates are approximate and provid an idea of the order of magnitude of change in cooling-rate between different samples.

3. Methods

3.1. Major element analyses of minerals and glass

Clinopyroxene and plagioclase compositions were measured using a JEOL 8200 Superprobe (Department of Earth Sciences, University of Geneva) at 15 nA, 15 kV with a spot size of 1 µm. For smaller clinopyroxenes, a Field Emission Gun JEOL JXA8530F Hyperprobe (School of Earth Sciences, University of Bristol) was used with 10 nA, 12 kV analytical conditions at a spot size <<1 µm. Calibration standards were natural and synthetic silicates or oxides. Na and K were measured first to mitigate diffusive migration. Counting time was 20 and 10 s on the peak and backgrounds respectively for Na and K, and 30 and 15 s for other elements. Measurements were corrected with the phi-rho-Z matrix

correction method (Armstrong, 1995). Olivine was analysed at 100 nA, 15 kV, with minor elements (Ca, Ni, Mn) measured for 100 s on peak and 50 s on backgrounds on both sides of the peak.

Quantitative element maps of plagioclase groundmass from sample 64R2 for FeO and MgO were made using the JEOL JXA8530F Hyperprobe with conditions of 12 kV and 100 nA, pixel sizes of 0.4×0.4 μm and a dwell time of 100 ms. Fe was measured on two spectrometers (LIFH and LIF crystals) and Mg was measured on three spectrometers (TAP crystals) before being summed to increase signal to noise ratio. Quantification of Fe and Mg was based on in-house plagioclase standards.

Major elements of glasses were measured with a JEOL JXA-8200 electron microprobe at GEOMAR, Kiel at 15 kV, 10 nA and a beam diameter of 5 μm. Counting times were 20/10 s (peak/background) for all elements apart for 30/15 s for K_2O, MnO, S, Cl and 40/20 s for F. Na_2O, S and Cl were measured first to avoid loss by heating of the beam. For calibration and monitoring of data quality, we used natural reference samples from the Smithsonian Institute (VGA99, VG2, Scapolite, KE3, ALV981; Jarosewich et al., 1980). The average was taken of nine analyses per sample to assure homogeneity and data quality. Relative analytical precision is generally better than 2.5%, but up to 5% for Na_2O, 10% for F, 30% for MnO and P_2O_5 and 50% for Cl and S.

3.2. Trace element analysis

In situ trace element abundances for clinopyroxene were analysed at the University of Lausanne, Switzerland, on a sector-field Inductively Coupled Plasma Mass Spectrometer ELEMENT XR interfaced to a New-Wave UP-193 ArF excimer ablation system using a 100–80 μm spot size, 10 Hz repetition rate, equivalent to a 6 J/cm^2 on-sample energy density. Sensitivity was optimized using the NIST SRM 612 glass standard ($^{139}La^+ = 3.5x10^6$ cps, $^{232}Th^+ = 5.0$–$5.5x10^6$ cps). During this optimization, doubly charged ions ($Ba^{2+}/Ba^+ < 2.7\%$) and oxide production rates ($ThO^+/Th^+ < 0.08\%$) were minimized. The NIST SRM612 glass standard was used during analysis and SiO_2 or CaO, measured previously on the microprobe, were used as internal standards. Data were processed using LAMTRACE (Jackson, 2008).

Additional trace element contents were determined on Au-coated thin sections using the NERC IMF Cameca ims-7f Geo ion microprobe at the University of Edinburgh. A primary beam of $^{16}O^-$ ions generated by a Hyperion RF source, an impact energy of 18 kV and a beam current of 0.06 nA was focussed onto the sample surface, resulting in a spot diameter of 2 μm. Secondary ions were accelerated to 5 kV without applying energy filtering (plagioclase) or using an energy window of 50 ± 20 V (clinopyroxene), and counted by a single EM detector. The instrument was set up for low mass resolution so as to maximise secondary ion transmission. Each clinopyroxene analysis consisted of 10 cycles measuring the following isotopes sequentially during each cycle: ^{23}Na, ^{24}Mg, ^{28}Si, ^{39}K, ^{49}Ti, ^{51}V, ^{88}Sr, ^{89}Y, ^{90}Zr, ^{138}Ba, ^{140}Ce. Count times were 1–2 s on major elements and 3–20 s on traces depending on concentration and isotopic abundance. For plagioclase a slightly different set of isotopes was measured (^7Li, ^{23}Na, ^{26}Mg, ^{28}Si, ^{39}K, ^{40}Ca, ^{49}Ti, ^{88}Sr, ^{90}Zr, ^{138}Ba). Prior to each analysis, the analytical area was pre-sputtered for ca. 120 s, during the last 60 s of which the secondary beam was aligned relative to the field aperture and mass calibration was updated using the ^{28}Si isotope in an automated software routine.

SIMS calibration for plagioclase was performed using an in-house standard (SPH1 labradorite) analysed independently by EPMA and LA-ICP-MS. Trace element signals were normalised to SiO_2 previously acquired by EPMA. Reproducibility of all elements in the standard ($n = 13$) was better than 3%, except Zr, at 5%, due to its low concentration (0.03 μg/g). Basaltic glass reference materials USGS GSE1-G and GSA1-G (TiO_2 only) were used for calibration of clinopyroxene analyses. Vanadium (at mass 51) suffers from molecular interferences ($^{24}Mg^{27}Al$, $^{26}Mg^{25}Mg$, $^{23}Na^{28}Si$), typically equivalent to about 20–30 ppm V, so a correction factor was calculated based on known V in GSA1-G. As

sample clinopyroxenes contain >800 ppm V, this correction is negligible. Clinopyroxene KH03–24 (Harvey et al., 2011) and basaltic glass reference material BCR2-G were used to monitor accuracy and precision, but it turned out that KH03–24 showed some major-element heterogeneity (MgO 15.2–16.8 wt%). Nevertheless, reproducibility was 2–8% for most elements except Zr (16%) which correlated with MgO and may therefore be heterogeneously distributed.

3.3. Modal abundances

Modal proportions of minerals in a selection of samples were acquired by processing SEM images with Image J (Schneider et al., 2012). Between three and six high-resolution SEM images (2560×1920 pixels) were acquired of representative textural domains on each sample using a Hitachi S-3500 N instrument (15 kV, 20 nA). We targeted groundmass areas without phenocrysts of olivine and plagioclase in order to quantify the abundances of clinopyroxene, plagioclase and oxides crystalizing in-situ during cooling. Glass is generally altered and only occasionally present in pillow rims. Proportions of oxides, plagioclase, clinopyroxene and altered glass were acquired by applying grey-scale thresholds to each image and measuring their respective proportions using Image J (*supplementary appendix*). In certain cases, only clinopyroxene and oxides were quantified due to alteration affecting plagioclase abundances. Our modes are reported as total proportions including alteration/glass (i.e. altered interstitial glass + occasional olivine phenocrysts) (Cpx + Plg + Ox + alteration products = 100) and alteration- and glass-free (Cpx + Plg + Ox = 100) (Fig. 3 and supplementary appendix).

3.4. Numerical modelling

We modelled the emplacement of lava flows of different thickness (1 to 10 m) (Fig. 4a) on the seafloor and computed the linear cooling rate across the lava flow between 1180 °C and near-solidus temperature of 1000–1050 °C (e.g., Thy et al., 1999). A temperature of about 1180 °C is estimated to be the emplacement temperature of these basaltic flows (see *Section 4*). We solved the heat conduction equation in the vertical dimension using a finite difference numerical method:

$$\partial T / \partial t = \kappa \bullet \Delta T$$

where ΔT is the variation in temperature following emplacement, t is the time and κ is the thermal diffusivity of a MORB from Hofmeister et al. (2016). At the beginning of the simulation, the substrate (assumed to be a previously emplaced MORB flow) is in thermal equilibrium with seawater (5 °C) and the lava flow has a homogeneous temperature of about 1200 °C. The top of the lava flow is maintained at 5 °C during cooling to account for seawater convection.

Synthetic Mg profiles in plagioclase were computed for various plagioclase growth rates (from 10^{-6} to 10^{-9} cm/s, Cashman, 1993) following the one-dimensional approach of Albarede and Bottinga (1972) and Smith et al. (1955) (Fig. 4b). The diffusivity of Mg (D_{Mg}) depends on temperature and melt composition (Zhang et al., 2010), and is therefore expected to vary during cooling and crystallization. For simplicity and to test the sensitivity of our model to varying diffusivities, we used fixed Mg diffusivities computed at temperatures of 1180 and 1120 °C (*see section 4*) as a function of melt composition following Zhang et al. (2010). The composition of the melt at those temperatures was approximated using MELTS models at a pressure of 0.3 kbar (*see section 4*) for a MORB corresponding to the measured average glass composition (*supplementary appendix*). The resulting Mg diffusivities at 1180 and 1120 °C are $3.4 \cdot 10^{-12}$ and $1.7 \cdot 10^{-12}$ m^2/s respectively (Fig. 4b). The partition coefficient of elements between plagioclase and melt depends on temperature, and melt and plagioclase compositions (Dohmen and Blundy, 2014). However, available partitioning data for Mg ($Kd_{Mg}^{plag-melt}$) obtained under comparable conditions as those of MORBs (see compilation in Dohmen and Blundy, 2014) reveal limited variations, with an
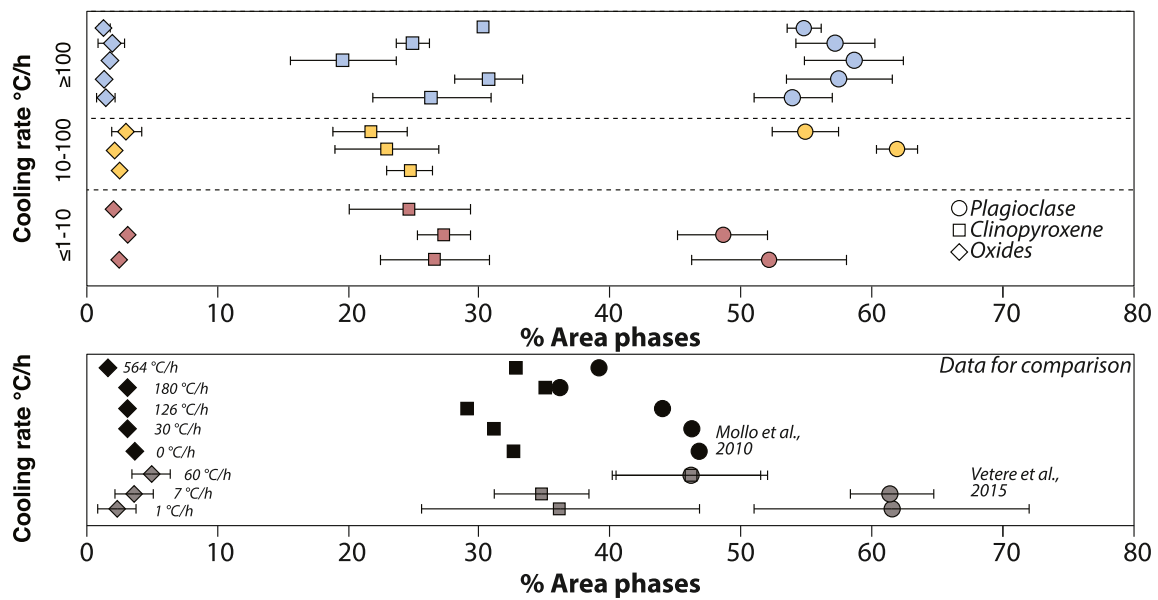
Fig. 3. Estimated mineral abundances (% area) of plagioclase, clinopyroxene and oxides from selected samples as a function of cooling rate. For comparison, modal phase abundances from cooling-experiments of Mollo et al. (2010) and Vetere et al., (2015).
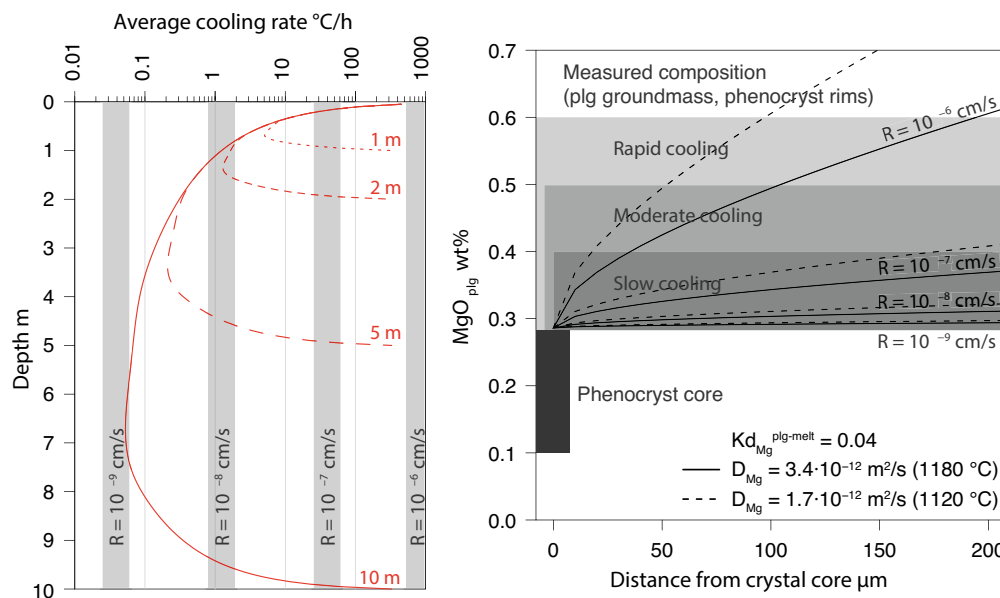

Fig. 4. (a) Average cooling rate of a basaltic lava flows of different thickness (1, 2, 5, 10 m) emplaced on the sea floor. Vertical grey fields represent the corresponding plagioclase growth rate (R) according to the empirical relationship of Cashman (1993); (b) Computed kinetic disequilibrium MgO profiles in plagioclase for various plagioclase growth rates following the one-dimensional approach of Albarede and Bottinga (1972) and Smith et al. (1955). Grey boxes correspond to the range of plagioclase composition at different cooling rates <1–10 °C/h (dark grey), 10–100 °C/h (intermediate grey) and ≥ 100 °C/h (light grey) (see Figs. 5 and 6). In (b), D: Mg diffusivity in the melt; $Kd_{Mg}^{plg\text{-}melt}$: Mg partition coefficient between plagioclase and melt (Dohmen and Blundy, 2014).

average $Kd_{Mg}^{plag\text{-}melt} = 0.04$, which was chosen for all simulations.

4. Results

4.1. Sample classification by cooling rate

Groundmass mineral proportions are $\leq 5\%$ for oxides, 20–40% for clinopyroxene and ≥ 45 plagioclase (Fig. 3). Aside from oxides, which show a slight decrease in abundance with increasing cooling rate in U1500 basalts (Fig. 3), the abundances of plagioclase and clinopyroxene do not show a significant change as a function of cooling rate, overlapping within error. Mineral proportions are broadly similar to cooling rate experiments (ca. 1–130 °C/h) of basalts (e.g., Mollo et al., 2010, Vetere et al. 2015) and of basaltic flows (Lesher et al., 1999) (Fig. 3). However, the lack of a shift in modal abundances with cooling rate is unlike experimental trends from Mollo et al., (2010) and Vetere et al.

(2015) (Fig. 3). This is likely a consequence of the sensitivity of nucleation and growth rates to small changes in P-T-fO$_2$-H$_2$O conditions of the crystallizing system (Mollo and Hammer, 2017). Nevertheless, the similar proportions of minerals in these lavas compared to experimental datasets suggest that natural and experimental datasets are broadly comparable.

Pillow lavas and external parts of massive flows (Fig. 1) show plagioclase with typical acicular, hopper/swallow-tail and skeletal habits forming bow-fanned to stellate textures while clinopyroxene is dendritic and interstitial, showing heterogeneous nucleation on elongated plagioclase. Oxides (magnetite) form late-stage flakes (<10 μm) typically nucleating on clinopyroxene tips (Fig. 2c). Such mineral textures imply elevated cooling rates (e.g., Lesher et al., 1999; Shea and Hammer, 2013) (Fig. 2). On the other hand, the internal parts of massive lava flows show individual grains of plagioclase becoming more prismatic and euhedral and faceted, and clinopyroxene showing coarser,

blocky faceted habits (Fig. 2c–e).

Based on similar dendritic, and elongated habits of plagioclase and clinopyroxene and intrafasciculated textures and comparison to experiments (Lesher et al., 1999; Del Gaudio et al., 2010; Mollo et al., 2011a, Mollo et al., 2011b) we can estimate a range of cooling rates of more rapidly cooled samples at ca. 100 °C/h, with an upper limit likely at ≥180 °C/h, when plagioclase probably disappears as a crystallizing phase (Vetere et al., 2015). The faceted, euhedral minerals in the more internal sections of U1500 lava flows are more consistent with cooling rates on the order of ≤10–50 °C/h (Fig. 2e,f) (e.g. Lesher et al., 1999; Mollo et al., 2011a, Mollo et al., 2011b, Del Gaudio et al., 2010; Giuliani et al., 2020). Moreover, calculated cooling rates for the emplacement of lava flows (Fig. 4a) decrease substantially over the first decimetre within the lava flow, with rapid cooling rates between 130 and 60 °C/h along the first 10 cm of the pillow basalt and slower cooling rates likely to occur along the centre of pillow lobs (ca. 10 °C/h). Cooling rates computed for the internal sections of thicker (ca. 5 m) lava flows are estimated to range at <1–10 °C/h.

Based on the texture of these basalts and comparison to experiments and our numerical modelling (Figs. 2, 4a), the studied samples represent a succession of rapidly cooled pillow lavas to slowly cooled internal sections of massive flows, recording a continuum in cooling rates from ca. 180 to <1 °C/h. We can therefore broadly subdivide our samples into *i)* holohyaline to hypohyaline quenched glassy margins containing plagioclase phenocrysts and no crystallized groundmass, forming the rims of basaltic pillows (Fig. 1c); *ii)* rapidly cooled basalts with cooling rate at ca. ≥100 °C/h, containing a groundmass of hopper plagioclase and dendritic to skeletal clinopyroxene (Fig. 2c); *iii)* moderately cooled basalts between ca. 10–100 °C/h, containing a groundmass of elongated plagioclase and coarser grained clinopyroxene with intermediate textures between slowly and rapidly cooled lava flows, representing predominantly the more external sections of individual massive lava flows (Fig. 2d); *iv)* slowly cooled basalts from the internal parts of lava flows at ca. <1–10 °C/h, with a groundmass of prismatic, euhedral plagioclase and coarse grained interstitial clinopyroxene and occasional comb-textured oxides (Fig. 2e).

4.2. Emplacement conditions of U1500 lava flows

Lava flows were recovered between 1400 and 1550 mbsf (meters below sea floor) and at a water depth of 3.8 km (Stock et al., 2018) (Fig. 1). Deep-marine trace fossils preserved in overlying sediments (Stock et al., 2018) indicate that eruption occurred at significant water depth. Eruption and crystallization pressure of the groundmass can therefore be estimated, using $P = h * d * g$ (g = 9.81 m/s^2, seawater density of 1025–1050 kg/m^3 (Talley, 2011), depth of max. 5.2 km), to range between 0.01 and 0.54 kbar. The lack of clinopyroxene xenocrysts/antecrysts combined with the abundance of plagioclase phenocrysts in these lava flows indicates low dissolved H$_2$O contents (Dungan and Rhodes, 1978; Grove et al., 1992; Feig et al., 2006), consistent with the low H$_2$O abundance of MORB (<0.8 wt%) (Michael, 1995; Sobolev and Chaussidon, 1996; Helo et al., 2011). RhyoliteMELTS calculations (Gualda et al., 2012) using an average glass composition (*supplementary appendix*), a crystallization pressure of 0.3–0.5 kbar and 0.2 wt% H$_2$O at QFM (quartz-fayalite-magnetite) fO$_2$ buffer indicate liquidus temperatures and the first appearance of plagioclase at 1188–1189 °C, followed by clinopyroxene (1170–1174 °C) and oxides at (1104–1108 °C), assuming equilibrium crystallization conditions (*supplementary appendix*). These temperatures are consistent with thermometers based on glass MgO abundances (eq. 13 of Putirka, 2008, which has an SSE of ±71 °C), which give us a temperature of 1183 ± 13 °C 2SD for these lava flows. Temperatures were also obtained using plagioclase-melt equilibrium (Eq. 24a with a SEE of ±36 °C, Putirka, 2008), by taking into consideration an average glass composition and plagioclase compositions with Kd$_{(Ab-An)}$ at ≥1050 °C of 0.27 ± 0.11 (Putirka, 2008). Calculated plagioclase-melt temperatures were uniform with cooling

rate: 1174 ± 6 °C (for samples at cooling rates of ≤1–10 °C/h), 1172 ± 5 °C (for samples at cooling rates of 10–100 °C/h) and 1172 ± 6 °C (for samples at cooling rates of ≥100 °C/h).

Therefore, this succession of lava flows represents the emplacement of homogenous plagioclase-olivine-phyric basalts at ca. 1180–1200 °C on the seafloor. Post-emplacement cooling led to crystallization of a groundmass formed of plagioclase followed by clinopyroxene and finally oxides, as shown by the textural relationships in these natural samples (Fig. 2).

4.3. Phase chemistry

4.3.1. Glass

Glass compositions remain homogenous throughout Hole 1500B, with Mg#$_{Fetot}$ varying between 54 and 59, SiO$_2$ between 50.5 and 59.0 wt%, and TiO$_2$ between 1.40 and 1.74 wt%. The composition of these basalts covers a small range within the Atlantic and Pacific MORB array (*supplementary appendix*).

4.3.2. Olivine

Olivine phenocrysts have molar % forsterite (Fo) varying between 79.7 and 88.2, Ni between 860 and 2050 ppm and Ca between 1745 and 2405 ppm. There are no identifiable variations in olivine composition between flows and repeat analyses indicate homogenous grains.

4.3.3. Plagioclase

Cores of plagioclase phenocrysts span the same range of compositions in all sections of all flows (Fig. 5). They are labradorite to bytownite in composition (An$_{56}$ to An$_{91}$), with relatively homogeneous and low MgO and FeO abundances (0.1–0.3 wt% and 0.2–0.6 wt% respectively). Groundmass plagioclase and rims of plagioclase phenocrysts, however, show important compositional variations between samples recording different cooling rates (Figs. 4, 5). Along the rims of lava flows and pillow lavas (≥100 °C/h), groundmass plagioclase shows restricted anorthite content (>An$_{55}$) but important variations in FeO and MgO at near-constant anorthite (Figs. 5a,d,g, 6 a-c). Samples within the centre of thicker lava flows (<1–10 °C/h) show a gradual increase in K$_2$O (reaching 0.2 wt%) as well as decreasing MgO (<0.05 wt%) with decreasing anorthite (down to An$_{34}$) (Figs. 5c,f,i, 6a-c). FeO abundances gradually increase up to 1 wt% with decreasing anorthite prior to rapidly decreasing at ca. An$_{45}$ (Fig. 5i). This shift in composition is also recorded in samples with intermediate cooling rates (10–100 °C/h) that have groundmass plagioclase compositions intermediate between both cooling rate endmembers (Figs. 5b,e,h, 6 a-c). Maximum measured anorthite contents for groundmass plagioclase gradually increase from An$_{81.3}$ (at <1–10 °C/h), to An$_{85.4}$ (at 10–100 °C/h) and finally to An$_{86.4}$ (at ≥100 °C/h) (Figs. 5, 6c). Microprobe mapping of groundmass plagioclase from rapidly cooled basalts highlights sector zoning controlled by changes in Fe and Mg abundances (Fig. 7). Similar sector zoning has previously been reported in groundmass plagioclase from pillow-lavas ("champagne glass zoning", Bryan, 1974).

SIMS analysis of trace elements of groundmass plagioclase confirm that MgO abundance are heterogeneous in plagioclase (*supplementary appendix*) whereas Ba (between 10 and 35 ppm), Sr (150 and 300 ppm) and TiO$_2$ (0.05 to 0.1 wt%) remain homogenous and do not vary between samples recording distinct cooling rates (Fig. 6 g-i).

4.3.4. Clinopyroxene

Changes in cooling rate of lava flows, as reflected in shifts in clinopyroxene morphology (Fig. 2), are also recorded in changes in clinopyroxene chemistry (Figs. 8, 9). Faceted clinopyroxenes from internal sections of lava flows (<1–10 °C/h) are typical of mid-ocean ridge gabbros, and are consistent with crystallization and in-situ melt differentiation, such as rapid decrease in Cr$_2$O$_3$ and Al$_2$O$_3$ and gradual increase in TiO$_2$ with decreasing Mg#$_{Fetot}$ (Fig. 8). Clinopyroxene shifts to higher Al$_2$O$_3$ (average of 3.2 to 4.3 wt%), TiO$_2$ (average of 1.3 to 2.8 wt
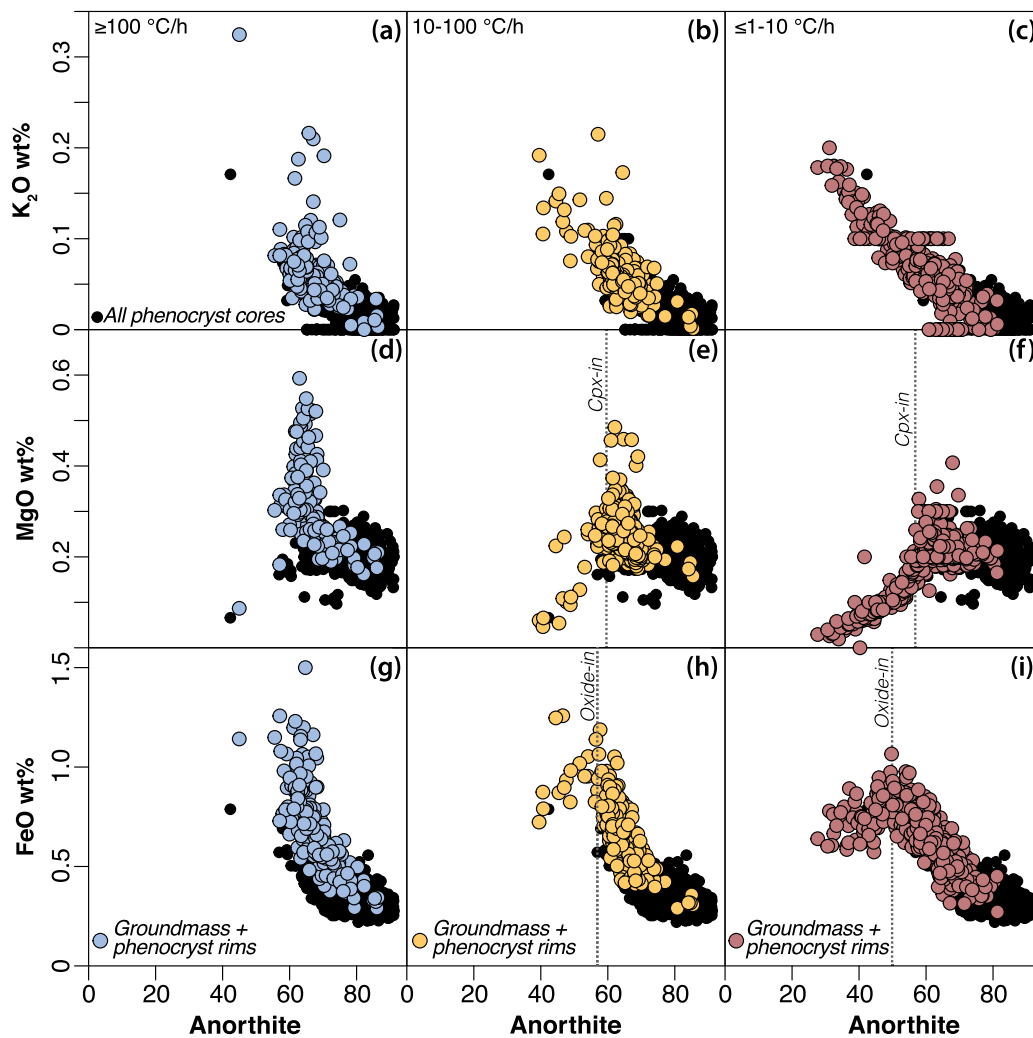
Fig. 5. Groundmass plagioclase composition illustrated by anorthite versus K_2O (a,b,c), MgO (d,e,f) and FeO (g,h,i). Plots are subdivided vertically by cooling rate: a, d,g: ≥ 100 °C/he; b,e,h: 10–100 °C/h; c,f,i: < 1–10 °C/h.

%) and Na_2O (average of 0.37 to 0.44 wt%) and decreasing $Mg\#_{Fetot}$ (average of 71.3 to 53.1) and SiO_2 (average of 50.1 to 46.4 wt%) (Figs. 8, 9) as cooling rates increase and clinopyroxene becomes more dendritic. These clinopyroxenes show a significant change in composition unlike that seen in crystallization experiments on dry tholeiites between 1 atm and 10 kbar (Grove et al., 1992; Villiger et al., 2007) which show a decrease in Al_2O_3 with decreasing $Mg\#_{Fetot}$ as well as a limited increase in TiO_2 with time (Fig. 8).

Trace element abundances in clinopyroxene are plotted in Figs. 10, 11. Slowly cooled blocky clinopyroxene have homogenous trace element abundances throughout the basalt flows, characterized by low abundances of Ce (<5 ppm), Y (<45 ppm), V (<800 ppm), Zr (<50 ppm) and Sr (<15 ppm). Trace element abundances increase sharply with increasing cooling rate, with dendritic clinopyroxene showing significant heterogeneity, e.g. Ce (5–30 ppm), Y (35–115 ppm), V (600–1400 ppm) Zr (50–300 ppm) and Sr (15–45 ppm) (Figs. 10, 11).

5. Discussion

5.1. Effect of cooling rate on plagioclase composition and Fe—Mg sector zoning

Our dataset records shifts in plagioclase composition over a range of cooling rates of ca. $1 - \geq100$ °C/h and offers a useful comparison to experimental work (e.g., Mollo et al., 2011a; Mollo et al., 2011b; Mollo

et al., 2012) (Fig. 6). Density distribution plots show a similar magnitude of increasing FeO and MgO as 1-atm cooling experiments between 2.5 and 150 °C/h (Fig. 6a-c), coinciding with similar changes in mineral textures (Mollo et al., 2012). Anorthite content seems somewhat less affected by changes in cooling rate compared to experiments of Mollo et al. (2012) and the density distribution of anorthite abundances remains well-defined and narrow for samples ≥10 °C/h (Fig. 6c). Nevertheless, maximum An abundances show a subtle increase with cooling rate (Fig. 6c) in line with 1-atm experiments of Mollo et al. (2012).

Although FeO and MgO uptake in plagioclase increases as a function of cooling rate, they show large variations at near-constant An (Fig. 5). This is due to groundmass plagioclase (at ≥100 °C/h) showing sector zoning formed of FeO- and MgO-enriched sectors (Fig. 7). This observation was initially made by Bryan (1974) in plagioclase from pillow lavas, with enrichment in FeO and MgO related to the (010) crystal faces. Near-constant anorthite abundance (~An_{60}) with increasing FeO and MgO implies that variation in anorthite content is not responsible for a modification of the plagioclase-melt partition coefficient (Dohmen and Blundy, 2014). Instead, sector zoning indicates that crystallization kinetics are involved in the incorporation of minor and trace elements in the growing crystal (Skulski et al., 1994) as rapid crystal growth will lead to the formation of a boundary layer enriched in slow-diffusing incompatible elements (Albarede and Bottinga, 1972; Bacon, 1989; Mollo et al., 2011a; Mollo et al., 2011b). This can be tested using the evolution of MgO abundances in plagioclase as a function of plagioclase
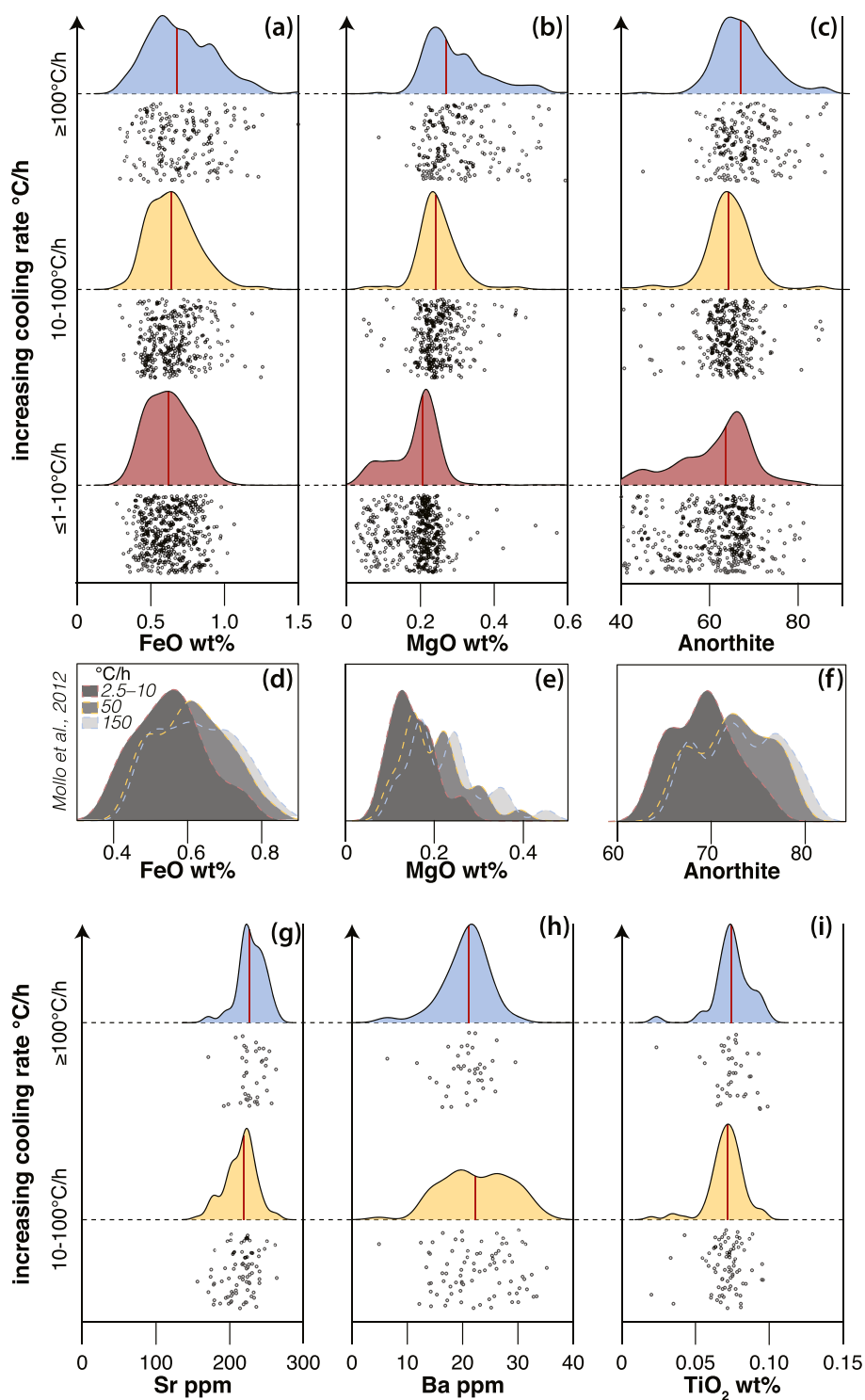
Fig. 6. (a-c) Density distribution and individual datapoints of FeO, MgO and anorthite in plagioclase from groundmass and phenocrysts rims as a function of cooling rate. (d-f) Density distribution of FeO, MgO and anorthite from 1-atm cooling experiments on basalt at variable cooling rates (2.5–10 °C/h, 50 °C/h and 150 °C/h respectively) (Mollo et al., 2012); (g-i) Density distribution and individual datapoints of Sr, Ba and TiO$_2$ in plagioclase from groundmass and phenocrysts rims as a function of cooling rate.

growth rates (Fig. 4b). Using a 1D growth model (Albarede and Bottinga, 1972), which is not inconsistent with the skeletal growth of plagioclase crystals (Figure 2:), and fixed temperatures (1180 °C and 1120 °C), we show that MgO sector zoning is unlikely to occur at growth rates below 10^{-7} cm/s (Fig. 4b). A sharp increase in MgO over 10s of microns from the crystal core is observed only at growth rates ca. 10^{-6} cm/s (Fig. 4b) and temperatures of 1180–1120 °C, covering the entire range of MgO abundances in groundmass plagioclase and showing similar sharp increases in MgO compared to quantitative profiles in Fig. 7. Such estimated growth rates cover the range of growth rates in volcanic systems

as inferred from crystal-size distribution studies of lava lakes, dykes and lava flows (Cashman, 1993) (Fig. 4).

Although our numerical model is limited by assumptions of constant temperature and growth rate, both of which will strongly influence the uptake of MgO (Fig. 4b), we can conclude that growth rates on the order of 10^{-6} cm/s are likely to lead to disequilibrium uptake of MgO in plagioclase. This suggests an initial stage of dendritic, swallow-tail structures at high growth rates ($\geq 10^{-6}$ cm/s); elevated FeO-MgO on (010) sectors) will be followed by in-filling and faceted near-equilibrium growth of plagioclase (low FeO-MgO) at lower growth rates (Fig. 7).
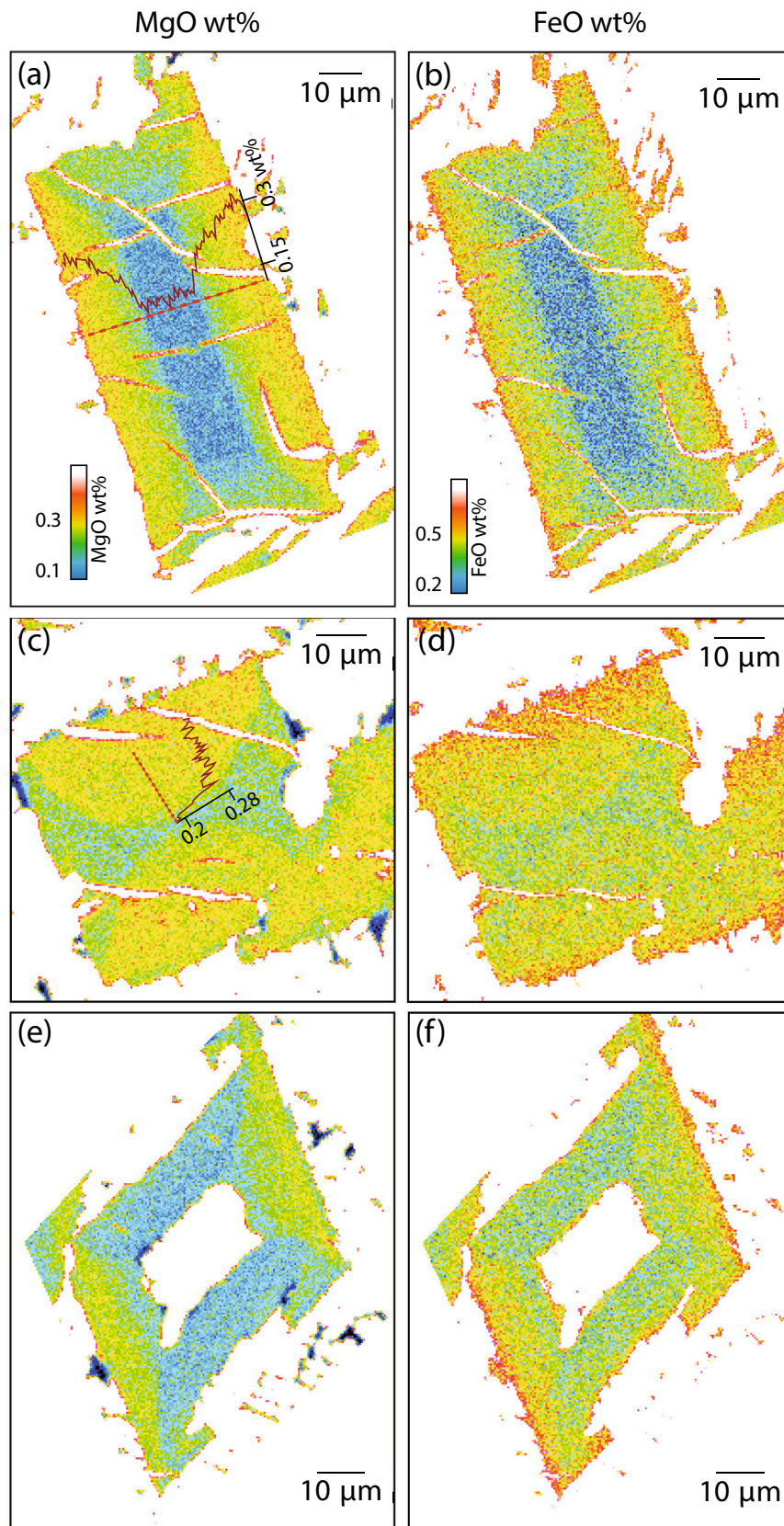
Fig. 7. (a-f) Quantitative microprobe maps of groundmass plagioclase in rapidly cooled lava flows showing well-defined MgO and FeO sector zoning; two quantitative profiles extracted with Image J on these plagioclase crystals show the rapid increase in MgO from core to rim along MgO-rich plagioclase crystal-faces.
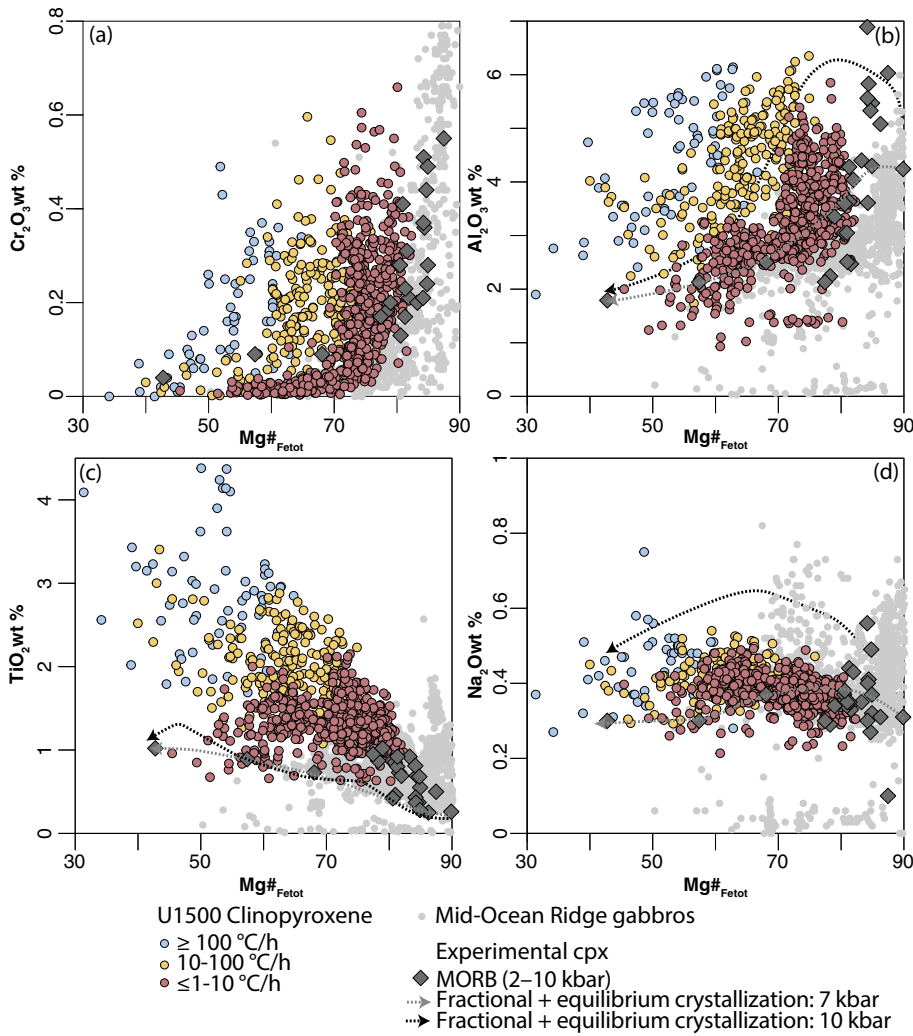
Fig. 8. Groundmass clinopyroxene composition as a function of Mg#$_{Fetot}$ and cooling rate: (a) Cr_2O_3, (b) Al_2O_3; (c) TiO_2; (d) Na_2O. Data for comparison for (ultra-) slow spreading systems (mid-ocean ridge gabbros) is a compilation from Müntener and McCarthy (2023). Experimental MORB clinopyroxenes are from dry tholeiitic basalts at 2, 8 and 10 kbar (Grove et al., 1992). Dotted lines represent fractional crystallization trends of clinopyroxene compositions of dry tholeiitic basalt at 7 and 10 kbar (after Villiger et al., 2007).
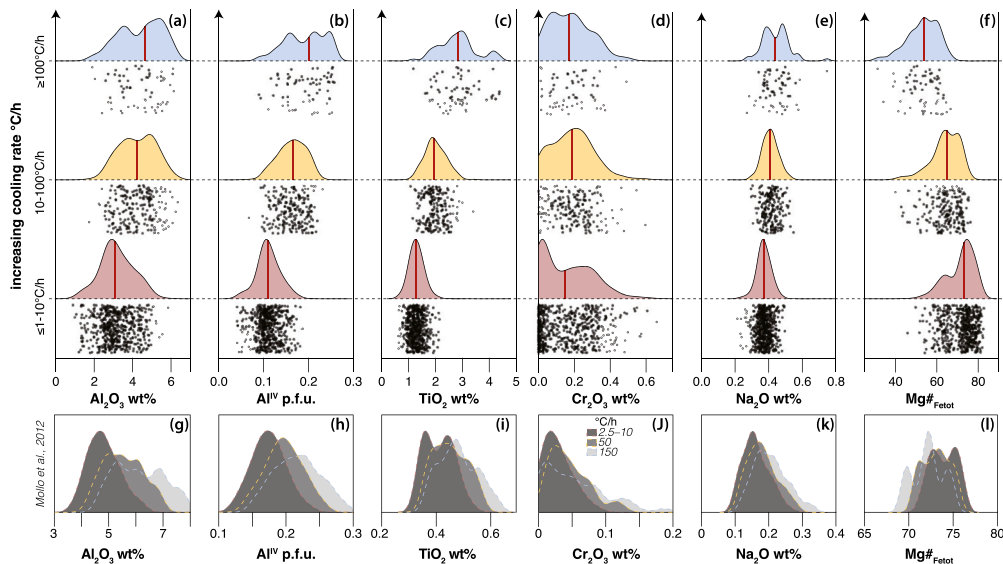

Fig. 9. Density distribution and individual datapoints of groundmass clinopyroxene as a function of cooling rate: (a) Al_2O_3; (b) Al^{IV}; (c) TiO_2; (d) Cr_2O_3; (e) Na_2O; and (f) Mg#$_{Fetot}$; (g-l) Density distribution of clinopyroxene composition from 1-atm cooling experiments on basalt as a function of cooling rate from Mollo et al. (2012).
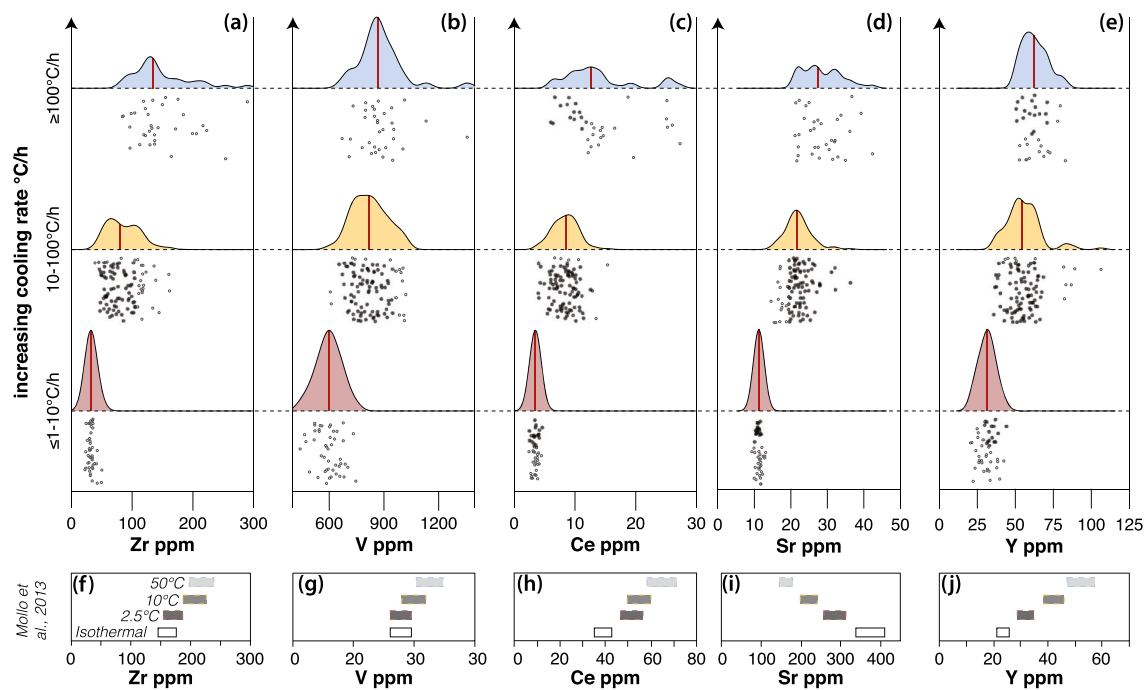
Fig. 10. Density distribution and individual datapoints of trace element abundances in groundmass clinopyroxene as a function of cooling rate: (a) Zr; (b) V; (c) Ce; (d) Sr; (e) Y; (f-j) Field of clinopyroxene composition from 1-atm cooling experiments on trachybasalt as a function of cooling rate from Mollo et al., (Mollo et al., 2013a; Mollo et al., 2013b).

Such high growth rates are not necessarily restricted to the outer rims of lava flows, dykes and tephras, and may be ubiquitous in subvolcanic systems, especially if degassing drives undercooling (e.g. Arzilli et al., 2015; McCarthy and Müntener, 2016; McCarthy et al., 2020), while even higher growth rates on the order of 10^{-5} cm/s might not be uncommon during the initial growth stage of phenocrysts (Welsch et al., 2016). Overall, this implies that MgO and FeO in plagioclase, particularly in (sub)volcanic systems, might record changes in growth rates (kinetics) in addition to any changes in fO_2 and/or melt composition (Longhi et al., 1976; Phinney, 1992; Singer et al., 1995; Ginibre et al., 2002; France et al., 2010).

SIMS analysis of Ba, Sr, Ti does not reveal any trends as a function of cooling rate (Fig. 6 g,h,i). Although trace element mapping of individual crystals by SIMS has not been done, our results might suggest that, under the natural conditions estimated for the basaltic samples object of this study, trace elements widely used to infer residence timescales of plagioclase, such as diffusion profiles of Sr and Ba (Dohmen and Blundy, 2014), are not significantly affected by changes in growth conditions. As the diffusivity of Mg in dry basaltic melts is higher than Sr and Ba (Zhang et al., 2010) the likely control on the presence of Mg zoning patterns lies in the higher incompatibility of Mg in plagioclase compared to Sr and Ba (Dohmen and Blundy, 2014).

5.2. The origin of oscillatory zoning in plagioclase

Changes in cooling rates (<1 to ≥100 °C/h), which affect growth rate over two orders of magnitude (Fig. 4a, Cashman, 1993), only lead to subtle shifts to higher anorthite content in plagioclase (Figs. 5, 6) (Mollo et al., 2012) and do not generate oscillatory zoning. This is particularly important as oscillatory zoning in plagioclase has been attributed to kinetic effects during crystal growth, either as a consequence of slow growth kinetics (Allègre et al., 1981) or rapid crystal growth (L'Heureux and Fowler, 1996; L'Heureux, 2013). Oscillatory zoning in accessory minerals, such as zircon, has also been interpreted in terms of interface kinetics (e.g. Hoskin, 2000). The lack of oscillatory zoning in plagioclase in the studied lava flows is consistent with the lack of oscillatory-zoned

plagioclase in experiments (e.g. Dohmen and Blundy, 2014; Del Gaudio et al., 2012; Mollo et al., 2012), a conundrum previously highlighted by Allègre et al. (1981) and Lasaga (1982), the latter showing that analytical solutions of plagioclase growth as a function of melt composition do not produce oscillatory zoning. Consequently, oscillatory zoning in plagioclase, a ubiquitous feature in a variety of magmatic systems (Singer et al., 1995; Ginibre et al., 2002; Blundy and Cashman, 2005; McCarthy et al., 2020), is difficult to explain solely in terms of growth kinetics. Instead, extrinsic processes are required, as plagioclase composition is strongly dependant on melt volatile content and temperature (Feig et al., 2006). For example, McCarthy et al. (2020) showed that extensive oscillatory zoning (5–15% An) in rapidly grown plagioclase glomerocrysts might result from rhythmic, syn-eruptive changes in melt volatile abundances as a consequence of volatile (CO_2, H_2O) fluxing through subvolcanic systems. Episodes of CO_2-fluxing might be relatively widespread, both in arc systems (Blundy et al., 2010) and along mid-ocean ridges (Helo et al., 2011). It is worth noting that plagioclase growth rates change by several orders of magnitude in magmatic systems (Kirkpatrick et al., 1979; Cashman, 1993; Muncill and Lasaga, 1987 and 1988; Barboni and Schoene, 2014; McCarthy et al., 2020, Antonelli et al., 2019), which implies that oscillatory zoning may reflect distinct processes occurring at different timescales. In contrast to syn-eruptive plagioclase glomerocrysts recording volatile fluxing on short (hourly) timescales (McCarthy et al., 2020), plagioclase in long-lived crystal-rich reservoirs (e.g. Caricchi and Blundy, 2015) might monitor magmatic processes occurring over longer timescales, including melt migration, variations in *P-T* conditions, magma-mixing and/or fluid percolation (e.g. Singer et al., 1995).

5.3. The effect of cooling rate on clinopyroxene composition

Clinopyroxene shows increasing Na_2O, TiO_2, Al_2O_3, Al^{iv} and lower Mg#$_{Fetot}$ with increasing cooling rate, spanning the entire range of clinopyroxenes from mid-ocean-ridge gabbros (Fig. 8). Cooling-rate experiments in basaltic systems at comparable conditions (2° – 150 °C/h) show remarkably similar trends (Fig. 9g-l) (Mollo et al., 2012) to these
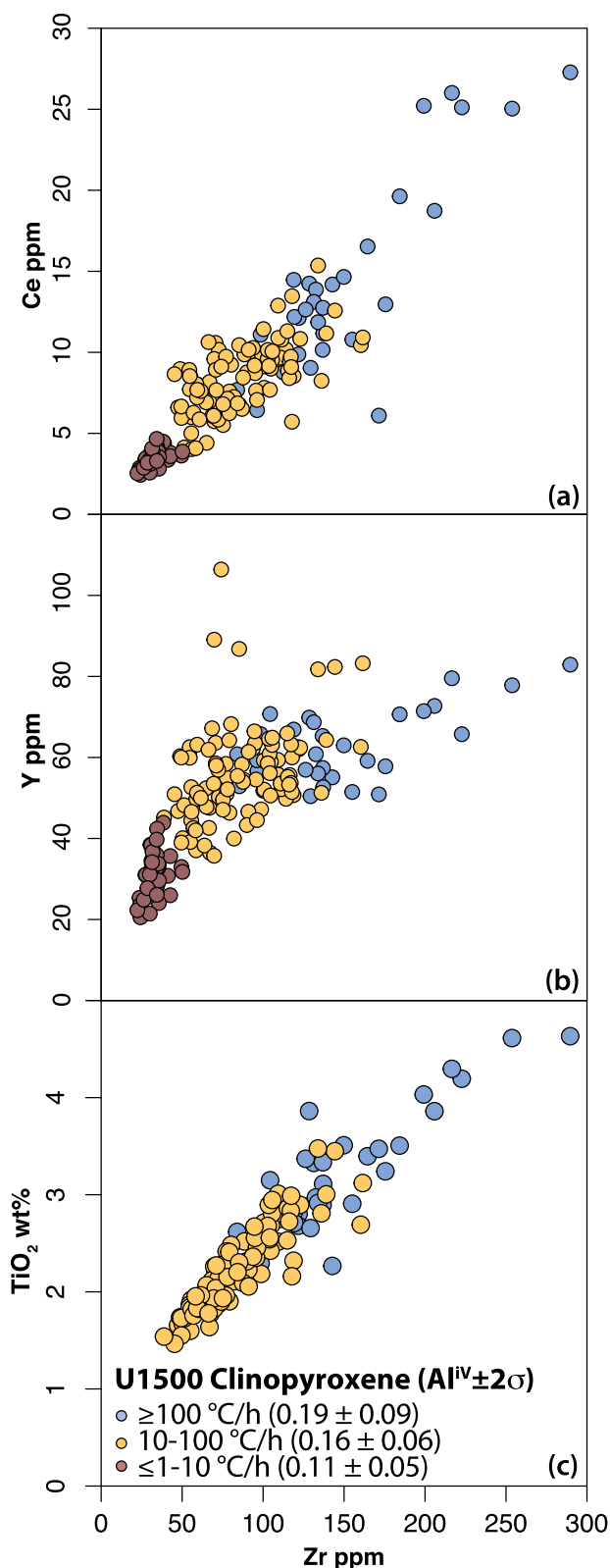
Fig. 11. Zr abundance in clinopyroxene as a function of (a) Ce, (b) Y and (c) TiO$_2$ and cooling rate.

through coupled substitution of ^{M1}(Al, Fe^{3+}) for ^{M2}(Mg,Fe^{2+}) and ^{T}Si^{4+} for ^{T}Al^{3+} (e.g. Etzel et al., 2007; Mollo et al., 2010, 2012). We also show that from ca. 10–100 °C/h to ca. ≥100 °C/h, Al$_2$O$_3$ and Al^{IV} abundances show only a limited increase (Fig. 9a,b), whereas TiO$_2$ increases significantly (Fig. 9c). This is likely a consequence of charge balance allowing for an increase in TiO$_2$ (Ti^{4+}) in the crystal structure (Mollo et al., 2012), and concomitant decrease in Mg#$_{Fetot}$ and Si (Figs. 8,9). Cr$_2$O$_3$, on the other hand, remains the only major or minor element unaffected by changes in cooling/growth rate and changes in Al—Ti abundances (Fig. 8a, Fig. 9d). Such patterns might imply that Cr$_2$O$_3$ abundances have potential as a record of melt replenishment or differentiation (e.g. Tornare et al., 2016; Ubide et al., 2019) independent of changes in crystal growth kinetics. However, it is worth noting that Cr zoning patterns might occur and be independent of enrichment or depletion in compatible and incompatible elements, as highlighted recently in experimental convective stirring conditions (Di Fiore et al., 2021).

Trace elements, such as Y, Ce, V, Zr, show similar initial enrichments with increasing cooling rates as experimental results from Mollo et al., (Mollo et al., 2013a, Mollo et al., 2013b) and a broad correlation with Al^{IV} (Fig. 11). Increasing Al in the crystal lattice facilitates charge-balanced incorporation of trace elements (Fig. 11) (Wood and Blundy, 2001; Mollo et al., 2013a; Mollo et al., 2013b), notably the highly-charged trace elements (Ce, Zr, Fig. 10) which increase by up to an order of magnitude (Lofgren et al., 2006). Apparent Kds calculated using bulk rock compositions of lava flows *(supplementary appendix)* show a significant increase with cooling rate for Ce, Zr, Y, and V, consistent with experiments (Mollo et al., 2013a, Mollo et al., 2013b) (Fig. 12). Although these natural samples reflect similar compositional trends with cooling rates to those observed experimentally (e.g. Mollo et al., 2011a; Mollo et al., 2011b; Mollo et al., 2013a; Mollo et al., 2013b), we note an
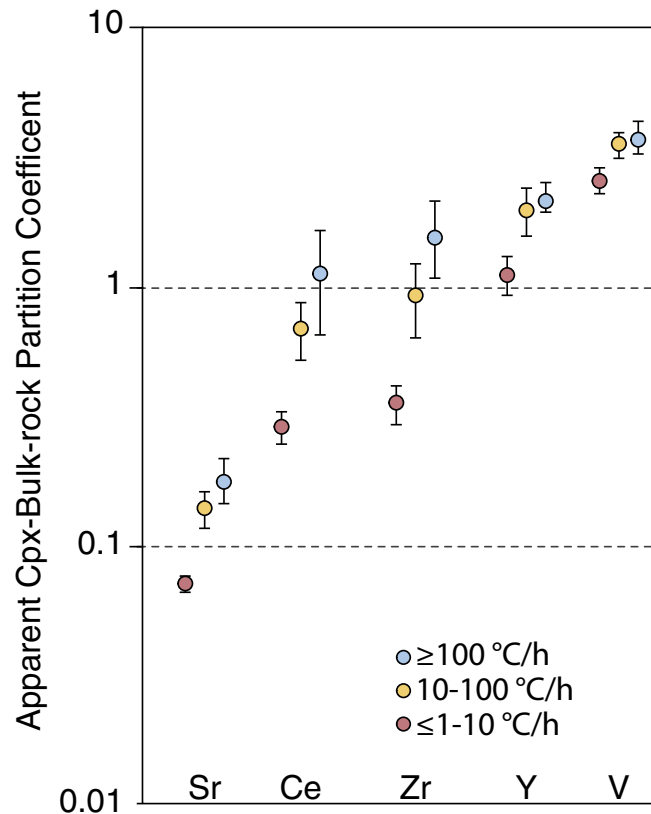
natural samples. As experimentally observed by Molllo et al. (Mollo et al., 2013a; Mollo et al., 2013b), the formation of boundary layers enriched in incompatible elements (Al$_2$O$_3$, TiO$_2$ and Na$_2$O) will lead to clinopyroxene with an increased Tschermak component (CaAl$_2$SiO$_6$)

Fig. 12. Apparent partition coefficients (Kd$^{cpx-melt}$, 1σ) based on groundmass clinopyroxene compositions and bulk rock chemistry of U1500 basalts *(supplementary appendix)* as a function of cooling rate.

increase in Sr abundance and apparent Kd, which is contrary of these experiments (Fig. 10). This is likely because the melt feeding the rapid growth of clinopyroxene in these experiments was depleted in Sr due to competition with adjacent plagioclase into which Sr is highly compatible.

One important result is the increasing compositional heterogeneity of clinopyroxene at elevated growth rates, in both major and trace elements (Figs. 8–11), at micron to submicron length-scales. One possibility is that increasing cooling rate leads to increased undercooling and increased nucleation rates (e.g. Shea and Hammer, 2013), with nucleation of metastable minerals favoured over stable phases (e.g. Kirkpatrick, 1983), thus favouring formation of compositionally variable Al-rich clinopyroxene (Shea and Hammer, 2013; Lofgren et al., 2006). An additional factor might be that kinetic effects locally influence the composition of nascent, rapidly growing crystals either related to boundary layers (e.g. Schwandt and McKay, 2006), or as a consequence of epitaxial growth of sub-micron minerals (e.g. oxides along clinopyroxene dendrites, Hammer et al., 2010) and their subsequent incorporation in the growing crystal. However, as the 2D – 3D structure of micron- to submicron-scale heterogeneity of these clinopyroxene is not resolvable (Fig. 2c), the different mechanisms cannot be elucidated. Nevertheless, slow solid-state diffusion of highly-charge trace elements in clinopyroxene means that heterogeneity, once formed, cannot be eliminated diffusively.

The heterogeneity in mineral compositions as a function of cooling rates highlighted here are noteworthy precisely because cooling rates of volcanic products depend on eruption conditions as well as the shape, size and permeability of volcanic fragments and thickness of lava flows, implying that mineral growth rates will vary by several orders of magnitude at small scales (Wallace et al., 2003; Cashman et al., 1999, Tait et al., 1998; Nichols et al., 2009). Our study on a series of natural lava flows shows significant changes in clinopyroxene and plagioclase compositions at small (i.e. hand-sample) scale, supporting extensive experimental work in recent years which has highlighted the sensitivity of both plagioclase and clinopyroxene chemistry and texture to changes in cooling rates. The sensitivity of clinopyroxene and plagioclase composition to growth rate implies that retrieving magmatic conditions on the basis of major and trace elements, or making correlations between distinct eruptions based on an array of scoria and lava flows, remains a hazardous task, as already highlighted by Mevel and Velde (1976).

6. Conclusions

Detailed analysis of mineral compositions in a 150 m thick submarine basalt lava flow sequence highlights the evolution of clinopyroxene and plagioclase compositions and textures as a function of cooling rate. Increasing cooling rates lead to plagioclase with higher FeO and MgO abundances and slightly higher An content, whilst Sr, Ba, Ti remain unaffected. Clinopyroxene is significantly more sensitive to changes in cooling rate, showing increasing Al–Ti–Na and decreasing Mg—Si contents with increasing cooling rate. Trace elements such as Y, V, Ce, Zr, Sr in clinopyroxene show an increase in abundance correlated with increased Al and especially Ti, and become more heterogeneously distributed. These shifts in mineral composition occur with increasing growth rates (10^{-9} to $\geq 10^{-6}$ cm/s) that overlap estimates for volcanic and subvolcanic magmatic systems. We show that plagioclase and clinopyroxene composition are sensitive to changes in growth rates, implying that the these mineral should be used with caution when discussing petrogenetic relationships in volcanic systems and use mineral chemistry to recover magmatic variables.

Supplementary data to this article can be found online at https://doi.org/10.1016/j.chemgeo.2023.121415.

Declaration of Competing Interest

The authors declare that they have no known competing financial interests or personal relationships that could have appeared to influence the work reported in this paper.

Data availability

Data will be made available on request.

Acknowledgments

References

Albarede, F., Bottinga, Y., 1972. Kinetic disequilibrium in trace element partitioning between phenocrysts and host lava. Geochim. Cosmochim. Acta 36, 141–156. https://doi.org/10.1016/0016-7037(72)90003-8.

Allègre, C.J., Provost, A., Jaupart, C., 1981. Oscillatory zoning: a pathological case of crystal growth. Nature 294 (5838), 223–228.

Antonelli, M.A., Mittal, T., McCarthy, A., Tripoli, B., Watkins, J.M., DePaolo, D.J., 2019. Ca isotopes record rapid crystal growth in volcanic and subvolcanic systems. Proc. Natl. Acad. Sci. 116 (41), 20315–20321.

Armstrong, J.T., 1995. CITZAF—a package of correction programs for the quantitative electron microbeam X-ray analysis of thick polished materials, thin-films and particles.: Microbeam. Analysis 4, 177–200.

Arzilli, F., Mancini, L., Voltolini, M., Cicconi, M.R., Mohammadi, S., Giuli, G., Mainprice, D., Paris, E., Barou, F., Carroll, M.R., 2015. Near-liquidus growth of feldspar spherulites in trachytic melts: 3D morphologies and implications in crystallization mechanisms. Lithos 216, 93–105.

Arzilli, F., Polacci, M., La Spina, G., Le Gall, N., Llewellin, E.W., Brooker, R.A., Torres-Orozco, R., Di Genova, D., Neave, D.A., Hartley, M.E., Mader, H.M., 2022. Dendritic crystallization in hydrous basaltic magmas controls magma mobility within the Earth's crust. Nat. Commun. 13 (1), 1–14.

Bacon, C.R., 1989. Crystallization of accessory phases in magmas by local saturation adjacent to phenocrysts. Geochim. Cosmochim. Acta 53 (5), 1055–1066.

Barboni, M., Schoene, B., 2014. Short eruption window revealed by absolute crystal growth rates in a granitic magma. Nature Geosci 7 (7), 524–528.

Blundy, J., Cashman, K., 2005. Rapid decompression-driven crystallization recorded by melt inclusions from Mount St. Helens volcano. Geology 33 (10), 793–796. https://doi.org/10.1130/G21668.1.

Blundy, J., Cashman, K.V., Rust, A., Witham, F., 2010. A case for CO2-rich arc magmas. Earth and Planet. Sci. Lett. 290 (3–4), 289–301.

Bryan, W.B., 1974. Fe-Mg relationships in sector-zoned submarine basalt plagioclase. Earth Planet. Sci. Lett. 24 (2), 157–165. https://doi.org/10.1016/0012-821X(74)90092-2.

Caricchi, L., Blundy, J., 2015. The temporal evolution of chemical and physical properties of magmatic systems. Geological Society, London, Special Publications 422 (1), 1–15.

Cashman, K.V., 1993. Relationship between plagioclase crystallization and cooling rate in basaltic melts. Contrib. Mineral. Petrol. 113, 126–142. https://doi.org/10.1007/bf00320836.

Cashman, K.V., Thornber, C., Kauahikaua, J.P., 1999. Cooling and crystallization of lava in open channels, and the transition of Pāhoehoe Lava to'A'ā. Bull. Volcanol. 61 (5), 306–323. https://doi.org/10.1007/s004450050299.

Del Gaudio, P., Mollo, S., Ventura, G., Iezzi, G., Taddeucci, J., Cavallo, A., 2010. Cooling rate-induced differentiation in anhydrous and hydrous basalts at 500 MPa: implications for the storage and transport of magmas in dikes. Chem. Geol. 270 (1–4), 164–178.

Di Fiore, F., Mollo, S., Vona, A., MacDonald, A., Ubide, T., Nazzari, M., Romano, C., Scarlato, P., 2021. Kinetic partitioning of major and trace cations between clinopyroxene and phonotephritic melt under convective stirring conditions: New insights into clinopyroxene sector zoning and concentric zoning. Chem. Geol. 584, 120531 https://doi.org/10.1016/j.chemgeo.2021.120531.

Di Genova, D., Brooker, R.A., Mader, H.M., Drewitt, J.W., Longo, A., Deubener, J., Neuville, D.R., Fanara, S., Shebanova, O., Anzellini, S., Arzilli, F., 2020. In situ

observation of nanolite growth in volcanic melt: a driving force for explosive eruptions. Sci. Adv. 6 (39), eabb0413.

Dohmen, R., Blundy, J., 2014. A predictive thermodynamic model for element partitioning between plagioclase and melt as a function of pressure, temperature and composition. Am. J. Sci. 314, 1319–1372. https://doi.org/10.2475/09.2014.04.

Donaldson, C.H., 1977. Laboratory duplication of comb layering in the Rhum pluton. Mineral. Magaz. 41 (319), 323–336.

Dowty, E., 1976a. Crystal structure and crystal growth: I. the influence of structure on morphology. Am. Mineral. 61, 448–459.

Dowty, E., 1976b. Crystal structure and crystal growth: II. Sector zoning in minerals. American Mineraloigst 61, 460–469.

Dungan, M.A., Rhodes, J.M., 1978. Residual glasses and melt inclusions in basalts from DSDP Legs 45 and 46: evidence for magma mixing. Contrib. Mineral. Petrol. 67, 417–431. https://doi.org/10.1007/BF00383301.

Etzel, K., Benisek, A., Dachs, E., Cemič, L., 2007. Thermodynamic mixing behavior of synthetic Ca-Tschermak–diopside pyroxene solid solutions: I. Volume and heat capacity of mixing. Physics and chemistry of Minerals 34, 733–746.

Feig, T.S., Koepke, J., Snow, J.E., 2006. Effect of water on tholeiitic basalt phase equilibria: an experimental study under oxidizing conditions. Contrib. Mineral. Petrol. 152, 611–638. https://doi.org/10.1007/s00410-006-0123-2.

France, L., Ildefonse, B., Koepke, J., Bech, F., 2010. A new method to estimate the oxidation state of basaltic series from microprobe analyses. J. Volcanol. Geotherm. Res. 189 (3–4), 340–346. https://doi.org/10.1016/j.jvolgeores.2009.11.023.

Ginibre, C., Wörner, G., Kronz, A., 2002. Minor-and trace-element zoning in plagioclase: implications for magma chamber processes at Parinacota volcano, northern Chile. Contrib. Mineral. Petrol. 143 (3), 300–315. https://doi.org/10.1007/s00410-002-0351-z.

Giuliani, L., Iezzi, G., Vetere, F., Behrens, H., Mollo, S., Cauti, F., Ventura, G., Scarlato, P., 2020. Evolution of textures, crystal size distributions and growth rates of plagioclase, clinopyroxene and spinel crystallized at variable cooling rates from a mid-ocean ridge basaltic melt. Earth-Science Rev. 204, 103165.

Grove, T.L., Kinzler, R.J., Bryan, W.B., 1992. Fractionation of mid-ocean ridge basalt (MORB). Mantle Flow and Melt Generation at Mid-Ocean Ridges 71, 281–310.

Gualda, G.A.R., Ghiorso, M.S., Lemons, R.V., Carley, T.L., 2012. Rhyolite-MELTS: a modified calibration of MELTS optimized for silica-rich, fluid-bearing magmatic systems. J. Petrol. 53, 875–890.

Hammer, J., Jacob, S., Welsch, B., Hellebrand, E., Sinton, J., 2016. Clinopyroxene in postshield Haleakala ankaramite: 1. Efficacy of thermobarometry. Contribut. to Mineral. Petrol. 171, 1–23.

Hammer, J.E., Sharp, T.G., Wessel, P., 2010. Heterogeneous nucleation and epitaxial crystal growth of magmatic minerals. Geology 38 (4), 367–370.

Harvey, J., Dale, C.W., Gannoun, A., Burton, K.W., 2011. Osmium mass balance in peridotite and the effects of mantle-derived sulphides on basalt petrogenesis. Geochim. Cosmochim. Acta 75 (19), 5574–5596. https://doi.org/10.1016/j.gca.2011.07.001.

Helo, C., Longpré, M.-A., Shimizu, N., Clague, D.A., Stix, J., 2011. Explosive eruptions at mid-ocean ridges driven by CO_2-rich magmas. Nat. Geosci. 4 (4), 260. https://doi.org/10.1038/NGEO1104.

Hofmeister, A.M., Sehlke, A., Avard, G., Bollasina, A.J., Robert, G., Whittington, A.G., 2016. Transport properties of glassy and molten lavas as a function of temperature and composition. J. Volcanol. Geotherm. Res. 327, 330–348. https://doi.org/10.1016/j.jvolgeores.2016.08.015.

Hoskin, P.W., 2000. Patterns of chaos: fractal statistics and the oscillatory chemistry of zircon. Geochimica et Cosmochimica Acta 64 (11), 1905–1923 (Vancouver).

Jackson, S.E., 2008. LAMTRACE data reduction software for LA-ICP-MS. In: Laser Ablation ICP-MS in the Earth Sciences: Current Practices and Outstanding Issues, p. 307.

Jarosewich, E., Nelen, J.A., Norberg, J.A., 1980. Reference samples for electron microprobe analysis. Geostand. Newslett. 4 (1), 43–47.

Kirkpatrick, R.J., Klein, L., Uhlmann, D.R., Hays, J.F., 1979. Rates and processes of crystal growth in the system anorthite-albite. J. Geophys. Res. Solid Earth 84 (B7), 3671–3676.

Kirkpatrick, R.J., 1983. Theory of nucleation in silicate melts. Am. Mineral. 68 (1–2), 66–77.

Lanzafame, G., Ferlito, C., 2014. Degassing driving crystallization of plagioclase phenocrysts in lava tube stalactites on Mount Etna (Sicily, Italy). Lithos 206, 338–347. https://doi.org/10.1016/j.lithos.2014.08.004.

Larsen, H.C., Sun, Z., Stock, J.M., Jian, Z., Alvarez Zarikian, C.A., Klaus, A., Boaga, J., Bowden, S.A., Briais, A., Chen, Y., Cukur, D., Dadd, K.A., Ding, W., Dorais, M.J., Ferré, E.C., Ferreira, F., Furusawa, A., Gewecke, A.J., Hinojosa, J.L., Höfig, T.W., Hsiung, K.-H., Huang, B., Huang, E., Huang, X.-L., Jiang, S., Jin, H., Johnson, B.G., Kurzawski, R.M., Lei, C., Li, B., Li, L., Li, Y., Lin, J., Liu, C., Liu, C., Liu, Z., Luna, A., Lupi, C., McCarthy, A.J., Mohn, G., Ningthoujam, L.S., Nirrengarten, M., Osono, N., Peate, D.W., Persaud, P., Qui, N., Robinson, C.M., Satoli, S., Sauermilch, I., Schindlbeck, J.C., Skinner, S.M., Straub, S.M., Su, X., Tian, L., van der Zwan, F.M., Wan, S., Wu, H., Xiang, R., Yadav, R., Yi, L., Zhang, C., Zhang, J., Zhang, Y., Zhao, N., Zhong, G., Zhong, L., 2018. Expedition 367/368 summary. In: Sun, Z., Jian, Z., Stock, J.M., Larsen, H.C., Klaus, A., Alvarez Zarikian, C.A. (Eds.), The Expedition 367/368 scientists. South China Sea Rifted margin. Proceedings of the International Ocean Discovery Program, 367/368: College Station, TX (International Ocean Discovery Program). https://doi.org/10.14379/iodp.proc.367368.101.2018.

Lasaga, A.C., 1982. Toward a master equation in crystal growth. Am. J. Sci. 282 (8), 1264–1288.

Lesher, C.E., Cashman, K.V., Mayfield, J.D., 1999. Kinetic controls on crystallization of tertiary North Atlantic basalt and implications for the emplacement and cooling history of lava at Site 989, Southeast Greenland Rifted margin. In: Larsen, H.C.,

Duncan, R.A., Allan, J.F., Brooks, K. (Eds.), Proceedings of the Ocean Drilling Program, Scientific Results, vol. 163.

L'Heureux, I., 2013. Self-organized rhythmic patterns in geochemical systems. Philos. Trans. R. Soc. A Math. Phys. Eng. Sci. 371 https://doi.org/10.1098/rsta.2012.0356.

L'Heureux, I., Fowler, A.D., 1996. Isothermal constitutive undercooling as a model for oscillatory zoning in plagioclase. Can. Mineral. 34 (6), 1137–1147.

Lofgren, G., 1974. An experimental study of plagioclase crystal morphology; isothermal crystallization. Am. J. Sci. 274 (3), 243–273. https://doi.org/10.2475/ajs.274.3.243.

Lofgren, G.E., Donaldson, C.H., 1975. Curved branching crystals and differentiation in comb-layered rocks. Contrib. Mineral. Petrol. 49 (4), 309–319. https://doi.org/10.1007/BF00376183.

Lofgren, G.E., Huss, R., Wasserburg, G.J., 2006. An experimental study of trace-element partitioning between Ti-Al-clinopyroxe and melt: Equilibrium and kinetic effects including sector zoning. Am. Mineral. 91, 1596–1606.

Longhi, J., Walker, D., Hays, J.F., 1976. Fe and Mg in plagioclase. In: Lunar and Planetary Science Conference Proceedings, 7, pp. 1281–1300.

Masotta, M., Pontesilli, A., Mollo, S., Armienti, P., Ubide, T., Nazzari, M., Scarlato, P., 2020. The role of undercooling during clinopyroxene growth in trachybasaltic magmas: Insights on magma decompression and cooling at Mt. Etna volcano. Geochimica et Cosmochimica Acta 268, 258–276. https://doi.org/10.1016/j.gca.2019.10.009.

McCarthy, A., Müntener, O., 2016. Comb layering monitors decompressing and fractionating hydrous mafic magmas in subvol- canic plumbing systems (Fisher Lake, Sierra Nevada, USA). J. Geophys. Res. Solid Earth 121 (12), 8595–8621. https://doi.org/10.1002/20 16jb013489.

McCarthy, A., Müntener, O., 2017. Mineral growth in melt conduits as a mechanism for igneous layering in shallow arc plutons: mineral chemistry of Fisher Lake orbicules and comb layers (Sierra Nevada, USA). Contrib. Mineral. Petrol. 172 (7), 55. https://doi.org/10.1007/s00410-017-1371-z.

McCarthy, A., Chelle-Michou, C., Blundy, J.D., Vonlanthen, P., Meibom, A., Escrig, S., 2020. Taking the pulse of volcanic eruptions using plagioclase glomerocrysts. Earth Planet. Sci. Lett. 552, 116596.

Mevel, C., Velde, D., 1976. Clinopyroxenes in Mesozoic pillow lavas from the French Alps: influence of cooling rate on compositional trends. Earth Planet. Sci. Lett. 32 (2), 158–164. https://doi.org/10.1016/0012-821X(76)90054-6.

Michael, P., 1995. Regionally distinctive sources of depleted MORB: evidence from trace elements and H_2O. Earth and Planet. Sci. Lett. 131 (3–4), 301–320.

Milman-Barris, M.S., Beckett, J.R., Baker, M.B., Hofmann, A.E., Morgan, Z., Crowley, M. R., Vielzeuf, D., Stolper, E., 2008. Zoning of phosphorus in igneous olivine. Contrib. Mineral. Petrol. 155 (6), 739–765. https://doi.org/10.1007/s00410-007-0268-7.

Mollo, S., Hammer, J.E., 2017. Dynamic crystallization in magmas. EMU Notes Mineral 16, 373–418.

Mollo, S., Del Gaudio, P., Ventura, G., Iezzi, G., Scarlato, P., 2010. Dependence of clinopyroxene composition on cooling rate in basaltic magmas: implications for thermobarometry. Lithos 118 (3–4), 302–312. https://doi.org/10.1016/j.lithos.2010.05.006.

Mollo, S., Lanzafame, G., Masotta, M., Iezzi, G., Ferlito, C., Scarlato, P., 2011a. Cooling history of a dike as revealed by mineral chemistry: a case study from Mt. Etna volcano. Chemical Geology 288, 39–52. https://doi.org/10.1016/j.chemgeo.2011.06.016.

Mollo, S., Putirka, K., Iezzi, G., Del Gaudio, P., Scarlato, P., 2011b. Plagioclase–melt (dis) equilibrium due to cooling dynamics: implications for thermometry, barometry and hygrometry. Lithos 125 (1–2), 221–235. https://doi.org/10.1016/j.lithos.2011.02.008.

Mollo, S., Misiti, V., Scarlato, P., Soligo, M., 2012. The role of cooling rate in the origin of high temperature phases at the chilled margin of magmatic intrusions. Chem. Geol. 322, 28–46.

Mollo, S., Scarlato, P., Lanzafame, G., Ferlito, C., 2013a. Deciphering lava flow post-eruption differentiation processes by means of geochemical and isotopic variations: a case study from Mt. Etna volcano. Lithos 162-163, 115–127. https://doi.org/10.1016/j.lithos.2012.12.020.

Mollo, S., Blundy, J.D., Iezzi, G., Scarlato, P., Langone, A., 2013b. The partitioning of trace elements between clinopyroxene and trachybasaltic melt during rapid cooling and crystal growth. Contrib. Mineral. Petrol. 166 (6), 1633–1654.

Muncill, G.E., Lasaga, A.C., 1987. Crystal-growth kinetics of plagioclase in igneous systems; one-atmosphere experiments and application of a simplified growth model. Am. Mineral. 72 (3–4), 299–311.

Muncill, G.E., Lasaga, A.C., 1988. Crystal-growth kinetics of plagioclase in igneous systems; isothermal H_2O-saturated experiments and extension of a growth model to complex silicate melts. Am. Mineral. 73 (9–10), 982–992.

Müntener, O., McCarthy, A., 2023. One View on the Petrology and Geochemistry of the Mantle and Oceanic Crustal Remnants in the Alps, Reconciling Rifts and Ultra-slow Seafloor Spreading. In: Geodynamics of the Alps 2. ISTE Ltd.

Nichols, A.R.L., Potuzak, M., Dingwell, D.B., 2009. Cooling rates of basaltic hyaloclastites and pillow lava glasses from the HSDP2 drill core. Geochim. Cosmochim. Acta 73 (4), 1052–1066.

O'Driscoll, B., Donaldson, C.H., Troll, V.R., Jerram, D.A., Emeleus, C.H., 2007. An origin for harrisitic and granular olivine in the Rum Layered Suite, NW Scotland: a crystal size distribution study. J.Petrol. 48 (2), 253–270.

Phinney, W.C., 1992. Partition coefficients for iron between plagioclase and basalts as a function of oxygen fugacity: implications for Archean and lunar anorthosites. Geochim. Cosmochim. Acta 56, 1885–1895.

Pontesilli, A., Masotta, M., Nazzari, M., Mollo, S., Armienti, P., Scarlato, P., Brenna, M., 2019. Crystallization kinetics of clinopyroxene and titanomagnetite growing from a

trachybasaltic melt: New insights from isothermal time-series experiments. Chem. Geol. 510, 113–129. https://doi.org/10.1016/j.chemgeo.2019.02.015.

Putirka, K.D., 2008. Thermometers and barometers for volcanic systems. Rev. Mineral. Geochem. 69 (1), 61–120.

Schneider, C.A., Rasband, W.S., Eliceiri, K.W., 2012. NIH image to ImageJ: 25 years of image analysis. Nat. Methods 9 (7), 671–675.

Schwandt, C.S., McKay, G.A., 2006. Minor-and trace-element sector zoning in synthetic enstatite. Am. Mineral. 91 (10), 1607–1615.

Shea, T., Hammer, J.E., 2013. Kinetics of cooling-and decompression-induced crystallization in hydrous mafic-intermediate magmas. J. Volcanol. Geotherm. Res. 260, 127–145.

Shimizu, N., 1990. The oscillatory trace element zoning of augite phenocrysts. Earth-Science Reviews 29 (1–4), 27–37.

Singer, B.S., Dungan, M.A., Layne, G.D., 1995. Textures and Sr, Ba, Mg, Fe, K, and Ti compositional profiles in volcanic plagioclase: clues to the dynamics of calc-alkaline magma chambers. Am. Mineral. 80 (7–8), 776–798.

Skulski, T., Minarik, W., Watson, E.B., 1994. High-pressure experimental trace-element partitioning between clinopyroxene and basaltic melts. Chem. Geol. 117 (1–4), 127–147.

Smith, V.G., Tiller, W.A., Rutter, J., 1955. A mathematical analysis of solute redistribution during solidification. Can. J. Phys. 33 (12), 723–745. https://doi.org/10.1139/p55-089.

Sobolev, A.V., Chaussidon, M., 1996. H2O concentrations in primary melts from supra-subduction zones and mid-ocean ridges: implications for H2O storage and recycling in the mantle. Earth Planet. Sci. Lett. 137 (1–4), 45–55.

Stock, J.M., Sun, Z., Klaus, A., Larsen, H.C., Jian, Z., Alvarez Zarikian, C.A., Boaga, J., Bowden, S.A., Briais, A., Chen, Y., Cukur, D., Dadd, K.A., Ding, W., Dorais, M.J., Ferré, E.C., Ferreira, F., Furusawa, A., Gewecke, A.J., Hinojosa, J.L., Höfig, T.W., Hsiung, K.-H., Huang, B., Huang, E., Huang, X.-L., Jiang, S., Jin, H., Johnson, B.G., Kurzawski, R.M., Lei, C., Li, B., Li, L., Li, Y., Lin, J., Liu, C., Liu, C., Liu, Z., Luna, A., Lupi, C., McCarthy, A.J., Mohn, G., Ningthoujam, L.S., Nirrengarten, M., Osono, N., Peate, D.W., Persaud, P., Qui, N., Robinson, C.M., Satolli, S., Sauermilch, I., Schindlbeck, J.C., Skinner, S.M., Straub, S.M., Su, X., Tian, L., van der Zwan, F.M., Wan, S., Wu, H., Xiang, R., Yadav, R., Yi, L., Zhang, C., Zhang, J., Zhang, Y., Zhao, N., Zhong, G., Zhong, L., 2018. Site U1500. In: Sun, Z., Jian, Z., Stock, J.M., Larsen, H.C., Klaus, A., Alvarez Zarikian, C.A. (Eds.), The Expedition 367/368 scientists, 2018. South China Sea Rifted margin. Proceedings of the International Ocean Discovery Program, 367/368: College Station, TX (International Ocean Discovery Program). https://doi.org/10.14379/iodp.proc.367368.104.2018.

Sun, Z., Jian, Z., Stock, J.M., Larsen, H.C., Klaus, A., Alvarez Zarikian, C.A., The Expedition 367/368 Scientists, 2018. South China Sea Rifted Margin. In: Proceedings of the International Ocean Discovery Program, 367/368: College Station, TX (International Ocean Discovery Program). https://doi.org/10.14379/iodp.proc.367368.2018.

Tait, S., Thomas, R., Gardner, J., Jaupart, C., 1998. Constraints on cooling rates and permeabilities of pumice in an explosive eruption jet from colour and magnetic mineralogy. J. Volcanol. Geotherm. Res. 86 (1–4), 79–91.

Talley, L.D., 2011. Descriptive Physical Oceanography: An Introduction, 6th edition. Academic Press.

Thy, P., Lesher, C.E., Mayfield, J.D., 1999. 9. Low pressure melting studies of basalt and basaltic andesite from the Southeast Greenland continental margin and the origin of dacites at Site 917. In: Larsen, H.C. (Ed.), Duncan. In Proceedings of the Ocean Drilling Program, Scientific Results, vol. 163, pp. 95–112. Ocean Drilling Program College Station.

Tornare, E., Pilet, S., Bussy, F., 2016. Magma Differentiation in Vertical Conduits Revealed by the Complementary Study of Plutonic and Volcanic Rocks from Fuerteventura (Canary Islands). Journal of Petrology 57 (11&12), 2221–2250. https://doi.org/10.1093/petrology/egx004.

Ubide, T., Caulfield, J., Brandt, C., Bussweiler, Y., Mollo, S., Di Stefano, F., Nazzari, M., Scarlato, P., 2019. Deep magma storage revealed by multi-method elemental mapping of clinopyroxene megacrysts at Stromboli volcano. Front. Earth Sci. 7, 239. https://doi.org/10.3389/feart.2019.00239.

Vetere, F., Iezzi, G., Behrens, H., Holtz, F., Ventura, G., Misiti, V., Cavallo, A., Mollo, S., Dietrich, M., 2015. Glass forming ability and crystallisation behaviour of sub-alkaline silicate melts. Earth-science reviews 150, 25–44.

Villiger, S., Ulmer, P., Müntener, O., 2007. Equilibrium and fractional crystallization experiments at 0.7 GPa—The effect of pressure on phase relations and liquid compositions of tholeiitic magmas. J. Petrol. 48 (1), 159–184. https://doi.org/10.1093/petrology/egl05.

Wallace, P.J., Dufek, J., Anderson, A.T., Zhang, Y., 2003. Cooling rates of Plinian-fall and pyroclastic-flow deposits in the Bishop Tuff: inferences from water speciation in quartz-hosted glass inclusions. Bull. Volcanol. 65, 105–123.

Watson, E.B., 1996. Surface enrichment and trace-element uptake during crystal growth. Geochim. Cosmochim. Acta 60 (24), 5013–5020. https://doi.org/10.1016/S0016-7037(96)00299-2.

Welsch, B., Hammer, J., Hellebrand, E., 2014. Phosphorus zoning reveals dendritic architecture of olivine. Geology 42 (10), 867–870. https://doi.org/10.1130/G35691.1.

Welsch, B., Hammer, J., Baronnet, A., Jacob, S., Hellebrand, E., Sinton, J., 2016. Clinopyroxene in postshield Haleakala ankaramite: 2. Texture, compositional zoning and supersaturation in the magma. Contrib. Mineral. Petrol. 171 (1) https://doi.org/10.1007/s00410-015-1213-9.

Wood, B.J., Blundy, J.D., 2001. The effect of cation charge on crystal-melt partitioning of trace elements. Earth Planet. Sci. Lett. 188, 59–71.

Zhang, Y., Ni, H., Chen, Y., 2010. Diffusion data in silicate melts. Rev Mineralogy Geochem 72, 311–408. https://doi.org/10.2138/rmg.2010.72.8.

Zhou, W., Van der Voo, R., Peacor, D.R., Zhang, Y., 2000. Variable Ti content and grain size of titanomagnetite as a function of cooling rate in very young MORB. Earth Planet. Sci. Lett. 179, 9–20.